THE ASTROPHYSICAL JOURNAL, 340:396–413, 1989 May 1

THE LATE BEHAVIOR OF SUPERNOVA 1987A. I. THE LIGHT CURVE

W. DAVID ARNETT[1]
Departments of Astronomy, Physics, and the Enrico Fermi Institute, University of Chicago
AND
ALBERT FU[2]
Department of Physics, Northwestern University
Received 1988 April 4; Accepted 1988 June 23

ABSTRACT

Theoretical models are compared to observations of the late (t = 20–1500 days) bolometric light curve and the γ-lines and X-rays from supernova 1987A. The analytic methods of Arnett (1982) are generalized to include recombination effects on opacity and energetics and are compared to numerical results. Enforcing constraints obtained from numerical work (Arnett 1987, 1988*b*) on the early observational data ($t < 20$ days), the effects of radioactive heating, gamma escape, and pulsar heating are examined.

The presence of $0.073 \pm 0.015\ M_\odot$ of freshly synthesized ^{56}Ni is needed to fit the bolometric light curve; the error estimate is dominated by uncertainty in the distance to the supernova. This matter must be well distributed in attenuation depth in the ejecta, as could be the case if the Rayleigh-Taylor instability encountered by Arnett (1987, 1988*a*) were operative, and/or clumping in density occurred. This modifies the light curve and predictions of X-ray and γ-ray escape. The γ-ray line flux is sensitive to the density and position of the radioactive matter; this may provide a constraint on the nature of the explosion.

The accurately exponential decay of the bolometric light curve for $t > 120$ days places severe limits on the luminosity ($L \leq 2 \times 10^{39}$ ergs s^{-1}) and the presumed period ($P \geq 2 \times 10^{-2}$ s) of the newly formed pulsar/neutron star. Some possible observational signatures of such an object are presented.

Subject headings: gamma rays: general — nucleosynthesis — stars: individual (SN 1987A) — stars: supernovae — X-rays: sources

I. INTRODUCTION

Analytic solutions have been developed which include the previously known behavior of Type I and II supernova light curves (Arnett 1980, 1982), as well as SN 1987A. They do not include the initial transient behavior, such as shock emergence, but become more realistic for later times. We apply these solutions to SN 1987A in order to analyze its nature and discuss some inherent weaknesses of numerical models to date.

In previous work (Arnett 1987*a*, 1988*a*, *b*; Nomoto, Shigeyama, and Hashimoto 1987; Woosley, Pinto, and Ensman 1988) it was shown that the early part ($t \leq 20$ days) of the observations of SN 1987A could be well understood as the explosion of a blue supergiant very similar to the identified progenitor, Sk $-69°+202$. The bolometric luminosity is well reproduced, with a rapid rise after the detection of neutrinos by Kamiokande II (Hirata *et al.* 1987) and IMB (Bionata *et al.* 1987), remaining below the Jones upper limit in the visual, and merging onto the flat plateau of the first weeks. In addition, the velocity structure (as inferred from P Cygni profiles) and the effective temperatures also agree well with observations. See Arnett (1988*a*, *b*) for a detailed discussion and references.

Using the characteristics of these models, Lucy (1987) has calculated synthetic spectra which give spectacular agreement with the observed spectra over the first week and slowly degrade over the second week. This suggests that some aspect of the physics or some of the parameters of the model require improvement. In this paper we investigate the later evolution of the supernova ($t \leq 1500$ days) both for its own intrinsic interest and also to better understand the nature of the star, its explosion, and its remnant, that is, to better define its parameters.

The early behavior of the explosion is determined in large part by two quantities: the size of the radiating surface and the strength of the shock which explodes it. The size is essentially fixed by the initial radius of the presupernova and is modified by the expansion velocity. The temperature of this surface is essentially fixed by the shock energy density, because the thermal energy density behind the shock is comparable to the corresponding kinetic energy density. Thus the temperature is also related to the expansion velocity.

To fit the observations, an initial radius $R = (3 \pm 1) \times 10^{12}$ cm and an energy density $E/M = (0.7 \pm 0.3) \times 10^{17}$ ergs g^{-1} were required. Note that this does not uniquely determine the mass M or the total explosion energy E, but only their ratio. As time passes, the observations provide information about deeper regions of the ejecta, so that a more complete picture of the event can be constructed, and in principle such ambiguity can be removed. Dopita (1988) has made a first step, estimating the shock-ejected hydrogen mass to be $5(+7, -3)\ M_\odot$.

The most obvious way to investigate the later behavior of the supernova is to continue the numerical computations to later times. This has been done, but it is found to suffer from two difficulties. First, numerical work of high quality makes heavy demands upon resources necessary to compute and to analyze the results; this presents special difficulty for a parameter study of the sort needed here. A second and more fundamental problem is that the numerical computations assume spherical symmetry, but they themselves indicate that this assumption is invalid. In a hydrostatic star, spherical sym-

[1] Supported by NSF grant AST8519968.
[2] Supported by NASA grant NAGW-768 and NSF grant AST8608291.

metry is maintained by the combined action of processes which tend to produce hydrostatic and thermal equilibrium. After the explosion these processes get out of phase. The density and composition structure essentially coasts (except for nonspherical motion; see below).

The temperature structure is more dynamic, being determined by the combined effects of cooling by expansion, cooling by radiative diffusion, heating by radioactivity, and heating by the underlying neutron star (a pulsar?). In a spherically symmetric computation a thermal cooling wave sweeps through a composition discontinuity in perfect phase around the spherical shell, giving rise to variation in radiative flow due to changes in opacity and ionization. There appears to be no mechanism to maintain this perfect phase coherence. On the contrary, the region initially rich in ^{56}Ni is heated by decay, and a pronounced Rayleigh-Taylor instability develops. This is at least one source for nonspherically symmetric motions, and macroscopic mixing can occur on the relevant time scales (microscopic mixing probably does not).

This is not the only mechanism for driving nonradial motions. Falk and Arnett (1973) predicted the development of a severe Rayleigh-Taylor instability and the presence of high- and low-density phases, even without the presence of radioactivity. Such a shock-initiated turnover does occur near the hydrogen-helium interface, for example. More generally, a pronounced tendency for clumping in density was found for accelerated matter when the thermal time scale approached the sound travel time.

While presenting this complication, the one-dimensional models also suggest a simplification: the global density structure of the presupernova is modified (by the shock) to have a simple form, the outer layers of which are preserved until times later than now for SN 1987A.

The outer part of the star ($\sim 1\%$ by mass) forms a power-law structure with $\rho = \rho_0(r_0/r)^n$ and $n = 9 \pm 3$. The inner part forms a region of (very roughly) uniform density; variation of ρ is of the order of a factor of 100, which is much smaller than the factor of 10^9 found in the power-law region (Arnett 1988*a*, *b*). At later times the inner part will dominate the light curve; as we shall see, the change occurs at ~ 20 days after the core collapse. Making idealized assumptions about the structure of this region—which cannot be treated correctly by one-dimensional numerical methods anyway—we can develop analytic models of the late part of the light curve and explore the characteristics of these simple cases more thoroughly.

We deal with the nonspherical motions by assuming that macroscopic mixing wipes out short-term transients such as those seen in the numerical computations; the good agreement with the observed light curves suggests that some such mechanism must be at work. We require that those parameters fixed by the numerical computations of the early light curve remain valid, so that we have a self-consistent description of both early and late behavior.

A direct comparison of analytic, numerical, and observational light curves is shown in Figure 1. The solid line represents the bolometric luminosity obtained from a continuation of the numerical computations (Arnett 1987, 1988*a*, *b*). The crosses show the bolometric light curve inferred by the SAAO group (Menzies *et al.* 1987; Catchpole *et al.* 1988). The analytic models (see below) are represented by a sequence of open circles; except for the transient behavior over the first 2 weeks, the analytic models agree with the observa-

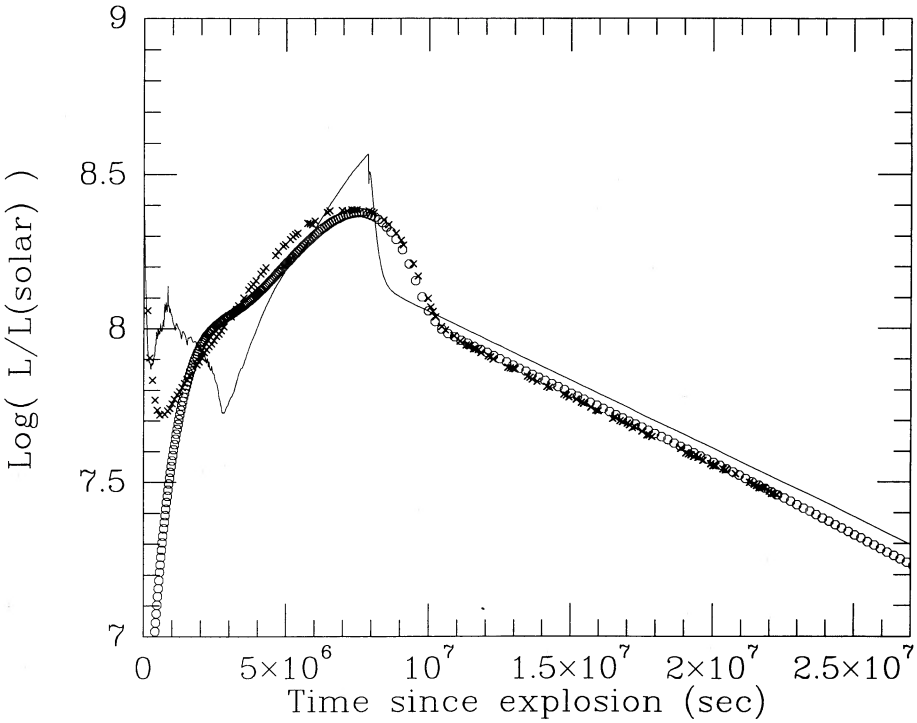

FIG. 1.—Bolometric luminosities: a comparison of analytic, numerical, and observational results. Solid line represents a continuation of the numerical computations of Arnett (1987, 1988*a*, *b*). Crosses show the bolometric light curve inferred by the SAAO group (Menzies *et al.* 1987; Catchpole *et al.* 1987). The analytic models are represented by a sequence of open circles; except for the transient behavior over the first 2 weeks, the analytic models agree with the observations significantly better than the numerical models.

tions significantly better than the numerical models. The excess luminosity after 120 days (10^7 s) seen in the numerical results is simply due to a slightly higher value assumed for the ^{56}Ni mass: 0.090 $M_\odot$ instead of 0.073.

Details of the generalization of the analytic procedure to include ionization fronts are presented in the Appendix.

II. GAMMA-RAY ESCAPE

A crucial feature of the late light curves is the decay of ^{56}Co. With decreasing density the gamma-ray escape becomes more likely. This changes the effective source term for heating the supernova matter and directly implies an increasing luminosity in gamma-ray line radiation and in X-radiation from Compton scattering of the gammas. This connection between the thermal radiation (in the infrared, visual, and ultraviolet), and the nonthermal radiation (in the X- and γ-ray bands) should become a key observational diagnostic of the supernova.

Previously (Arnett 1982) the effects of gamma-ray loss were treated on the basis of the analytic representation of numerical computations of escape from a uniform sphere of 0.75 $M_\odot$ with 0.25 $M_\odot$ of ^{56}Ni, which was given by Colgate, Petschek, and Kriese (1980). An external mass of 0.75 $M_\odot$ of H and He did not alter their results much. Those parameters were chosen for a Type I supernova.

Here we consider 0.1 $M_\odot$ or so of ^{56}Ni and a total mass of 6–20 $M_\odot$; for this rather different parameter range we have recalculated gamma-ray loss using numerical methods (see Fu and Arnett 1989 for details). We find a convenient representation of these results by means of a Schuster-Schwarzschild model for gamma attenuation and use this analytic approximation for nonuniform distribution of density and of ^{56}Ni.

The approximation is derived as follows: take the conventional expression for energy loss (wavelength shift) from Compton scattering (e.g., Richtmeyer, Kennard, and Lauritsen 1955) and integrate over scattering angle. If the "average photon" has energy ϵ_i after the ith scatter, then following the $(i+1)$th scatter the energy is $\epsilon_{i+1} = \epsilon_i/(1 + \epsilon_i/mc^2)$. If we start with a gamma-ray energy of 0.847 MeV, this sequence of energies is given in Table 1.

This is a measure of the change of the energy distribution of gamma rays upon downscatter. Note the large energy loss on the first scatter, and the small fractional loss as the energy decreases. To scatter down to 8 keV (the K-edge for absorption in Ni or Co) requires $\sim$60 scatters. The last scatter reduces the energy by $\sim$1.6%, to be compared with 62.4% on the first.

The heating may be represented by a dominant component within one mean free path of the source, and a more diffuse one spreading out to $(60)^{1/2} \approx 8$ mean free paths. For simplicity in our analytic model we assume that each newly created gamma ray moves radially outward or inward, and that its interaction is governed by exponential attenuation with the Klein-Nishina cross section for its birth energy. This "one-shot" procedure may be thought of as a Schuster-Schwarzschild attenuation model; it captures the main features of the numerical computations with fair accuracy (see Fu and Arnett 1989). Because of its simplicity it can be easily integrated for a given distribution of radioactive matter and of density.

TABLE 1

AVERAGE ENERGIES OF COMPTON-SCATTERED PHOTONS

Number of Scatters	Average Energy (MeV)
0	0.847
1	0.319
2	0.196
3	0.142
4	0.111
5	0.0912
6	0.0774

The escape function so computed allows a direct estimate of the escaping gamma rays, and hence of the gamma-ray line luminosities. In retrospect we find that the mathematical errors in this approximation are smaller than the real uncertainties in the physical parameters relating to the distribution of the source and the attenuating mass.

The depth τ_γ for gamma rays is

$$\tau_\gamma = \int_0^R \rho\kappa\, dr\ , \tag{1}$$

and if we choose a constant opacity κ (Klein-Nishina for example) and a dimensionless density function η (see Appendix), we have

$$\tau_\gamma = \tau(0)_\gamma [R(0)/R(t)]^2\ , \tag{2}$$

where

$$\tau(0)_\gamma = \rho(0,0)\kappa_{KN} R(0) I_\tau\ , \tag{3}$$

and

$$I_\tau \equiv \int_0^1 \eta(x)\, dx\ . \tag{4}$$

In what follows it is important to include the effect of extra electrons per nucleon for hydrogen-rich matter. We do this by using an average over the whole mass of ejecta.

If the radioactive nucleus has an initial mass fractional abundance $X_{Ni}(0)$ and is uniformly distributed out to a fractional radius $x = b$, the total mass of this nucleus is

$$M_{Ni} = \int_0^{bR} X_{Ni}(0) 4\pi\rho r^2\, dr = 4\pi\rho(0,0) R(0)^3 I_{Ni} X_{Ni}(0)\ , \tag{5}$$

where

$$I_{Ni} \equiv \int_0^b \xi(x)\eta(x) x^2\, dx\ . \tag{6}$$

Here $\xi(x)$ is the dimensionless function describing the shape of the distribution of radioactive nuclei. Similarly, the total mass M is

$$M = 4\pi\rho(0,0) R(0)^3 I_M\ , \tag{7}$$

where

$$I_M \equiv \int_0^1 \eta(x) x^2\, dx\ , \tag{8}$$

and

$$M_{Ni}/M = X_{Ni}(0) I_{Ni}/I_M\ . \tag{9}$$

For a newly born gamma ray at x, the probability that it escapes on a radial "upward" trajectory is $e^{-\tau(1-x)}$, and for a radial "downward" trajectory is $e^{-\tau(1+x)}$. If we divide the new gamma rays into equal up and down beams, we arrive at the

escape integral I_e given by

$$I_e = \int_0^b e^{-\tau}(e^{\tau x} + e^{-\tau x})(\tfrac{1}{2})\xi(x)\eta(x)x^2\,dx\,. \quad (10)$$

Because the integration is over a source term consisting of the radioactive nuclei, the integration is limited accordingly. A spherical shell of ^{56}Co would be represented by the same expression with a finite lower bound.

The density distribution for the numerical model of Arnett (1988*a*) at 18 days may be approximated crudely by

$$\eta(x) = e^{-ax}\,, \quad (11)$$

where $a \approx 4.6$. We will use this form for illustrative purposes. The model actually has more complex structure, and this structure itself will be modified by Rayleigh-Taylor instability. Even in the spherically symmetric approximation the structure will change with time and may be different for various mechanisms for the explosion.

Let us define a useful function $f(y)$ by

$$f(y) \equiv 2 - e^{-y}(2 + 2y + y^2)/y^3\,. \quad (12)$$

With this simple form for $\eta(x)$, and taking $\xi(x) = e^{-cx}$,

$$I_M = f(a)\,, \quad (13)$$

$$I_\tau = (1 - e^{-a})/a\,, \quad (14)$$

$$I_{\rm Ni} = b^3 f[(a + c)b]\,, \quad (15)$$

$$I_e = I_+ + I_-\,, \quad (16)$$

where

$$I_+ \equiv b^3[\![f\{[(a + c) + \tau_\gamma]b\}]\!]\,. \quad (17)$$

and

$$I_- \equiv b^3 f\{[(a + c) - \tau_\gamma]b\}\,. \quad (18)$$

We can now construct a general deposition function (see Appendix),

$$D(t) = I_e/I_{\rm Ni}\,, \quad (19)$$

which is a function of time through τ_γ, and of the structure parameters a, b, and c.

Unlike attenuation, diffusion is relatively insensitive to density structure (Arnett 1980). Relatively small differences in density structure may modify the degree of gamma attenuation significantly, with little effect on the thermal light curve. We may take advantage of this by using uniform density to estimate the thermal light curve, and including only the density variation in the attenuation calculation (where it is most important).

III. BEHAVIOR OF ANALYTIC LIGHT CURVES

Connecting a numerical model of the early light curve with an analytic model of the late light curve is not trivial because (1) the numerical model is not homologous at early times, as must be assumed for the analytic model, and (2) the velocity of the inner regions of the numerical model is sensitive to the inner boundary condition, which does not seem to have been done correctly as yet (this relates to the uncertainty concerning the explosion mechanism).

To be specific, we approximate the inner 99% of the ejected mass with an analytic model using the constants given in Table 2.

TABLE 2

VALUES OF CONSTANTS USED

Quantity	Value
v_{sc}^2	$3.333E_{sn}/M_{ej}$
$E_{th}(0)$	$E_{sn}/2$
τ_{Ni}	7.604×10^5 s
β	13.7
ϵ_{Ni}	3.89×10^{10} ergs g^{-1} s^{-1}
τ_{Ni}/τ_{Co}	0.07743
I_{th}	0.1013
κ (0.847 MeV)	0.344 $\kappa_{Thomson}$

We examine two series of models, having total ejected masses of 7.5 and 15 $M_\odot$, respectively. The corresponding standard parameters are given in Table 3. Notice the effective radius R_0 is a measure of the ratio of kinetic to initial thermal energy for the analytic models and need not directly correspond to the radius, which contains 99% of the ejected mass at the time of explosion. When taken with velocity, it is also a measure of the rate of expansion cooling. The values shown are close to estimated values from the numerical models and have a mass sensitivity which may ultimately be used to constrain the ejected mass. Note also the assumption that the ^{56}Ni (or ^{56}Co) is mixed out through 0.4 of the "radius of the uniform density ejecta." This corresponds to a velocity of only 1789 km s^{-1} for these models, which is comparable to that of the hydrogen/helium interface; Arnett (1988*a*, *b*) found the hydrogen abundance to start at a velocity of 1300 km s^{-1} and to reach its maximum value above 3100 km s^{-1}. The velocity at the midpoint in the transition region was 2000 km s^{-1}. The opacity is chosen to represent that in the opaque regions near 100 days, which are the inner regions of the ejecta. It is important to include the effect of extra electrons per nucleon on the gamma attenuation in hydrogen-rich regions.

a) *The Effect of Changes in Initial Radius*

We would like to take the value of R_0 simply to be the inferred radius of the presupernova star. For accurate quantitative work, this is inadequate for two reasons. First, the analytic solutions are valid only after the star has settled to homologous expansion, which requires a factor of 5 increase in its radius. Second, the presence of radioactivity gives heating which modifies the velocity and density structure with time, changing the effect of expansive cooling, and hence the effective "initial radius."

The effect of different R_0 is shown in Figure 2. The solid points represent the data from SAAO (Menzies *et al.* 1987; Catchpole *et al.* 1988, and private communication). The lines

TABLE 3

VALUES OF PARAMETERS USED

Quantity	Model 7.5	Model 15
Mass ejected	7.5 $M_\odot$	15 $M_\odot$
H mass ejected	3 $M_\odot$	10.5 $M_\odot$
Energy (E_{sn})	1.0×10^{51} ergs	2.0×10^{51} ergs
Effective R_0	1.05×10^{12} cm	0.75×10^{12} cm
Mass (^{56}Ni)	0.075 $M_\odot$	0.075 $M_\odot$
κ_t	0.20	0.20
T_{ion}	5500 K	5500 K
Q_{ion}	33.6 eV	33.6 eV
Density scale a	0.0	0.0
^{56}Ni radius b	0.4	0.4

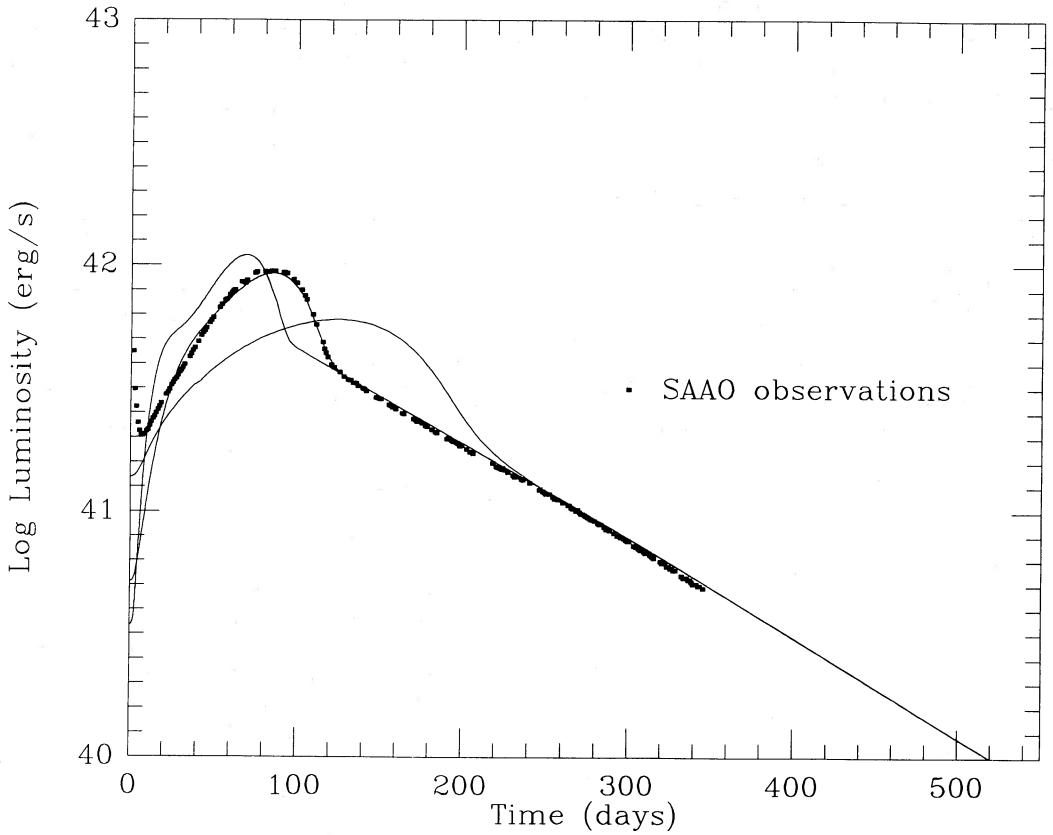

FIG. 2.—Bolometric light curve for an injected mass of 15 $M_\odot$. Solid lines represent the bolometric luminosity of *thermal* radiation; luminosity due to escaping gamma-rays and X-rays is treated separately. The three curves represent three choices of effective initial radius, with the slowest and dimmest peak corresponding to the largest radius. These curves are to be compared with the SAAO data (*solid dots*); the primary uncertainties in the observational data are due to assumptions concerning extinction, reddening, and distance to the LMC.

represent the model with ejected mass of 15 $M_\odot$ for $R_0 = 0.5$, 0.75, and 2.0×10^{12} cm. The $R_0 = 0.5 \times 10^{12}$ cm curve has an ugly bump at 20 days and falls below the observations around 100 days, giving an unacceptable fit. The $R_0 = 2.0 \times 10^{12}$ cm curve has a peak which is much too short and broad. The $R_0 = 0.75 \times 10^{12}$ cm curve is difficult to distinguish from the observed points, except for the first 25 days when the ignored transient solution dominates. That epoch is well represented by the earlier numerical calculations (Arnett 1987, 1988*a*, *b*).

We may now compare this inferred R_0 with an equivalent numerical model in which the early hydrodynamics is computed in detail. At a time of 3.25×10^3 s, the homology ratio (of velocity to radius) is $v/r \approx 2.0 \times 10^{-4}$ over most of the ejecta, as may be seen in Figure 3. Because $v/r = v/(R_0 + v_{sc}\, t)$, this implies $R_0 = 0.82 \times 10^{12}$ cm, which is slightly above the values we just found from the light curve for this model. Note that this effective R_0 is approximately one-third of the actual initial radius of the precursor star; we may use this ratio to convert model values of R_0 to actual precursor radii.

In Figure 4, the model with ejected mass of 7.5 $M_\odot$ is used to show the effect of different R_0. The lines represent the luminosity for $R_0 = 0.5$, 1.0, and 2.0×10^{12} cm. The $R_0 = 0.5 \times 10^{12}$ cm curve has lost the ugly bump at 20 days, but peaks too early. The $R_0 = 2.0 \times 10^{12}$ cm curve again has a peak which is much too short and broad. The $R_0 = 1.05 \times 10^{12}$ cm curve is relatively good, but has a peak which is a bit too short. Interestingly enough, this is opposite to the problem of the numerical light curve shown in Figure 1. All these curves sag below the observational data (and the exponential decay expected from radioactive decay) after 280 days; this is due to gamma escape, which will be examined in detail below. This sag can be cured by keeping the ^{56}Co more attenuated, i.e., under more of the matter. Fu and Arnett (1989) show that the simple algorithm we use here for gamma-ray escape errs on the side of too much escape, so that the quantitative agreement for these parameters is slightly better than it appears.

Notice that this value of R_0 is 40% larger than in the previous case, and since the scaling velocity remains fixed, this implies an early luminosity which is also 40% larger. To fit the observations with this set of parameters, the distance to SN 1987A would have to be 20% larger than assumed; alternatively, the explosion energy would be reduced, possibly giving velocities smaller than observed. Similarly, an ejected mass much larger than the previous value of 15 $M_\odot$ would require a lower value of R_0, and imply a dimmer and therefore closer SN 1987A.

b) The Effect of Changes in Mass, Opacity, and Velocity

The effect of differing values of mass, opacity, and velocity on the light curve may be best understood by first considering a slightly simpler problem. Previously (Arnett 1982) analytic solutions were found for the diffusion of radioactively deposited energy through an expanding sphere, and they were used to describe light curves of Type I supernovae. In those models the dominant decay was that of ^{56}Ni. The nature of the light

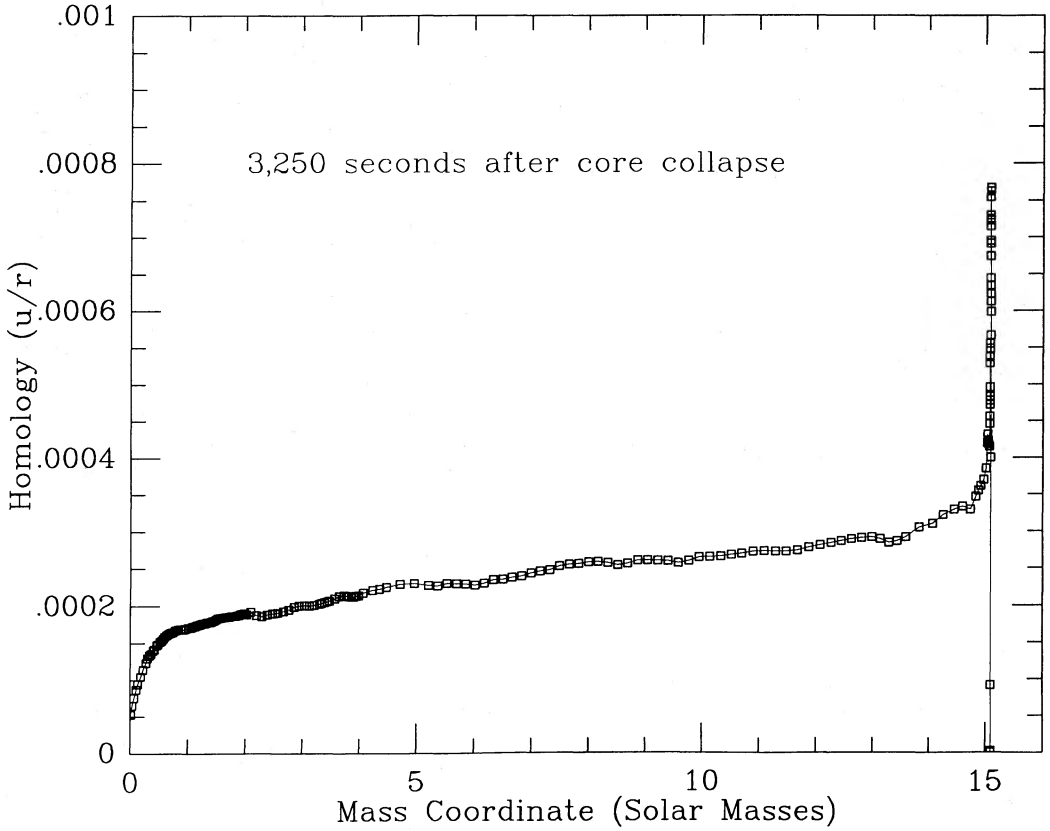

FIG. 3.—Expansion homology ratio v/r vs. mass coordinate at an early time of 3250 s after core collapse. The units are inverse seconds and solar masses, respectively. Near the surface and the origin the expansion is not homologous with the bulk of the matter.

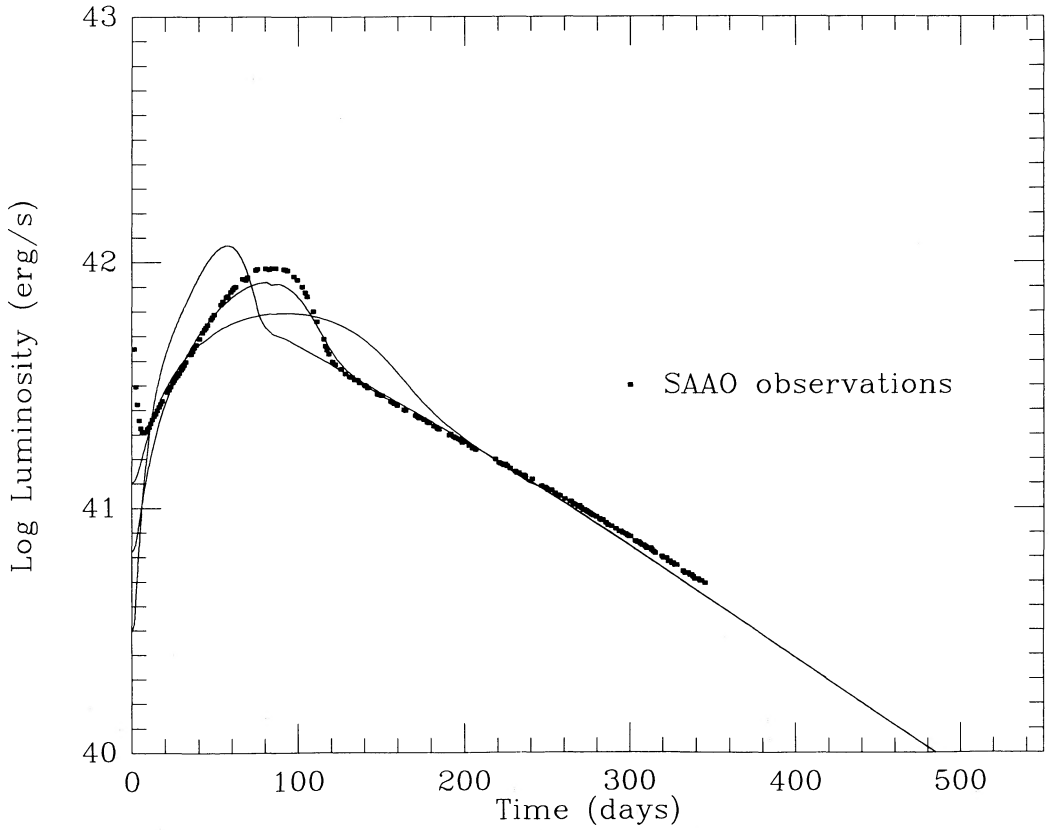

FIG. 4.—Bolometric light curve for an ejected mass of 7.5 $M_{\odot}$. The notation is the same as for Fig. 2. The most significant difference with the previous figure is the increased transparency to gamma-rays. This causes the thermal light curve to sag below the radioactive energy line at a time near 280 days.

curves was determined by a dimensionless parameter y,

$$y = \tau_m / 2\tau_{\rm Ni} , \tag{20}$$

where

$$\tau_m^2 = 2\tau_0 / \tau_h , \tag{21}$$

the time scale for hydrodynamic expansion is

$$\tau_h = R_0 / v_{\rm sc} , \tag{22}$$

and the time scale for radiative diffusion is

$$\tau_0 = \frac{9}{4\pi^3} \frac{\kappa M}{c R_0} . \tag{23}$$

Therefore the parameter y is the ratio of the geometric mean of the hydrodynamic and the diffusion times to the decay, time, and

$$y^2 = \frac{9}{8\pi^3} \frac{\kappa M}{c v_{\rm sc} \tau_{\rm Ni}^2} , \tag{24}$$

so that the R_0 dependence cancels out. Increasing the factor $\kappa M / v_{\rm sc}$ will make the peak broader and dimmer for these solutions; decreasing it will give faster, brighter light curves.

Consider how this parameter y will change from the Type I case to that of SN 1987A. The opacity is larger by 1.5, the mass is larger by 10, and the decay time is larger by 12.9, giving a value of y which is smaller by a factor of 0.53. The Type I case used $y \approx 1.0$, for which the maximum occurred around two decay times ($x = 1$ in the notation of Arnett 1982). For $y \approx 0.5$ the maximum occurs around 1.2 decay times (see Table 1 in Arnett 1982), or ~ 135 days. The observed peak is at 80–90 days, as may be seen in Figures 2 and 4.

Direct examination shows such models for SN 1987A to be inconsistent; the effective temperature drops well below the recombination temperature of hydrogen. At such low temperatures the matter becomes transparent. This is equivalent to a decrease in the factor κM above, and makes faster and brighter light curves, as Figures 2 and 4 demonstrate. It is recombination that introduces a dependence of the light curve on the initial radius R_0.

As it was for Type I supernovae, the parameter y is crucial for understanding the shape and duration of the light curve of SN 1987A. We find that a great variety of parameter variations can be succinctly understood in terms of changes in the value of this parameter. A given value of y can be obtained from a variety of combinations of mass, opacity, and velocity. The removal of this ambiguity requires that additional information be used.

c) *The Effect of Different Recombination Temperatures*

In view of the previous discussion, it is interesting to see how the light curves change for different assumed temperatures of recombination; this is shown in Figure 5 for the model with ejected mass of 15 $M_\odot$. The parameters are standard (Table 3) except for recombination temperature. The broad curve is for no recombination; it peaks around 120 days, which is consis-

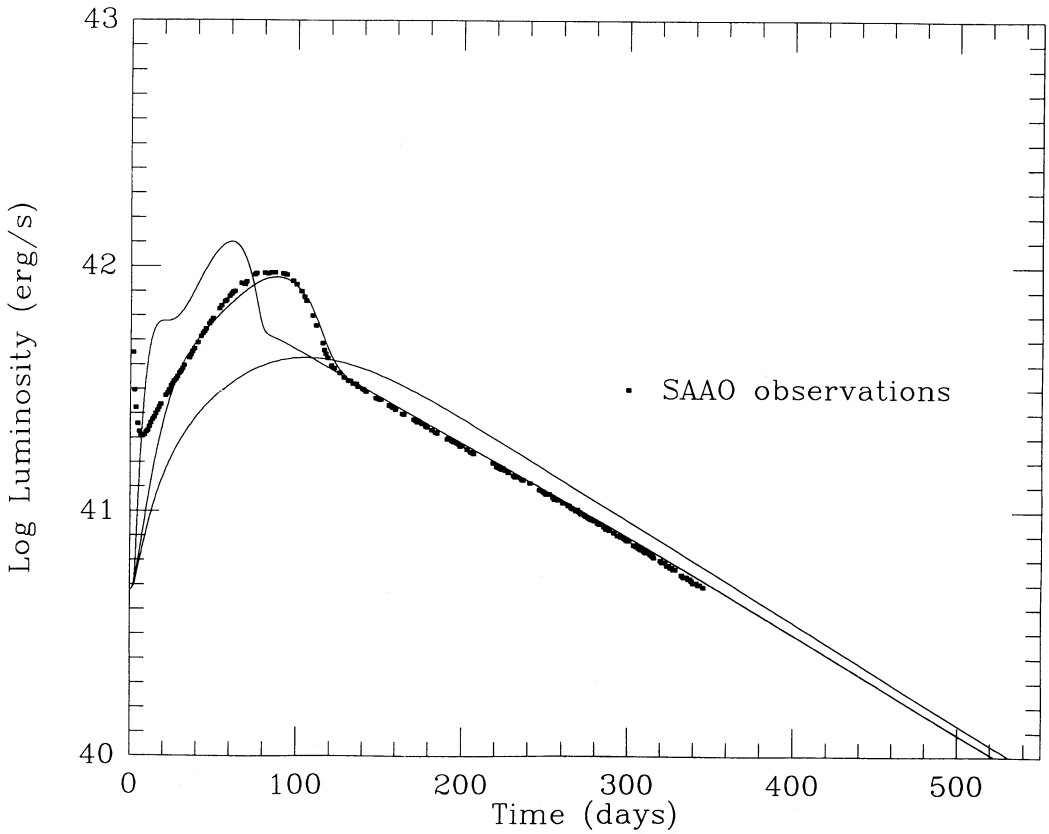

FIG. 5.—Bolometric light curve for an ejected mass of 15 $M_\odot$, for different choices of recombination temperature. The notation is the same as for Fig. 2. The standard curve is shown, for which $T_{\rm recom} = 5500$ K. The fast curve, with a more pronounced peak, corresponds to 11,000 K. The slow curve corresponds to no recombination and provides a measure of the importance of this effect.

tent with our rough estimate above. The fast, bright curve is for an assumed recombination temperature of 11,000 K.

For SN 1987A the recombination temperature is essentially an observable quantity in that it approaches the effective temperature as the matter becomes transparent. Our standard choice of 5500 K is a rough average of the observed effective temperature over the first 100 days.

d) The Effect of Different Density Structure

The bolometric light curve for thermal radiation shown in Figure 4 showed a sag below the observations after 280 days. From the discussion in § II above, we expect that this may be modified by different density structure. Figure 6 shows this to be the case. Our standard choice of uniform density is shown; it is the lowest curve. For the middle curve, the density varies as $\rho \propto \exp(-x)$, while for the higher curve the dependence is $\rho \propto \exp(-2x)$. Only the "sag" in the exponential tail is sensitive to these rather mild changes; the gamma attenuation involves the density distribution in an exponential function, while thermal diffusion does not. We see that the behavior of the light curve after 120 days probes the innermost regions of the supernova ejecta.

In order to get agreement with the observations, the density variation had to be chosen so that it was higher in the inner regions in which most of the radioactive nuclei were contained. Radioactive heating would tend to cause expansion, thus reducing the local density rather than increasing it. A tentative conclusion is that this value of the ejected mass is too small. Comparison of multidimensional hydrodynamic calculations with observational data should decide this point.

e) The Effect of Different Ionization Energy

Average ionization energies per nucleon of 11.6, 33.6, and 100 eV per nucleon are shown as the lower, middle, and higher curves in Figure 7. Note that the curves differ only around the peak. An inhomogeneous distribution of composition could modify the shape of the peak; approximating the ionization energy with an average value tends to spread the peak more than a realistic distribution, which would have heavier elements nearer the center.

Using the approximation quoted in the Appendix (see eq. [A45]), the ionization energy per nucleon for pure ^{4}He would be 21 eV and that for pure ^{16}O would be 133 eV.

IV. GAMMA-RAY LINES

The detection of gamma-ray line emission from SN 1987A (Matz *et al.* 1987, 1988; Sandie *et al.* 1988; Cook *et al.* 1988; Rester *et al.* 1988) represents crucial information for analyzing the event. Escaping gamma rays will be Compton-scattered down to X-ray energies. The detection of X-rays by *Ginga* (Dotani *et al.* 1987) and *Mir* (Sunyaev *et al.* 1987) provide a complementary constraint on the physics of the phenomena. These data will be considered in more detail in Fu and Arnett (1989); here we examine them as constraints on the nature of SN 1987A.

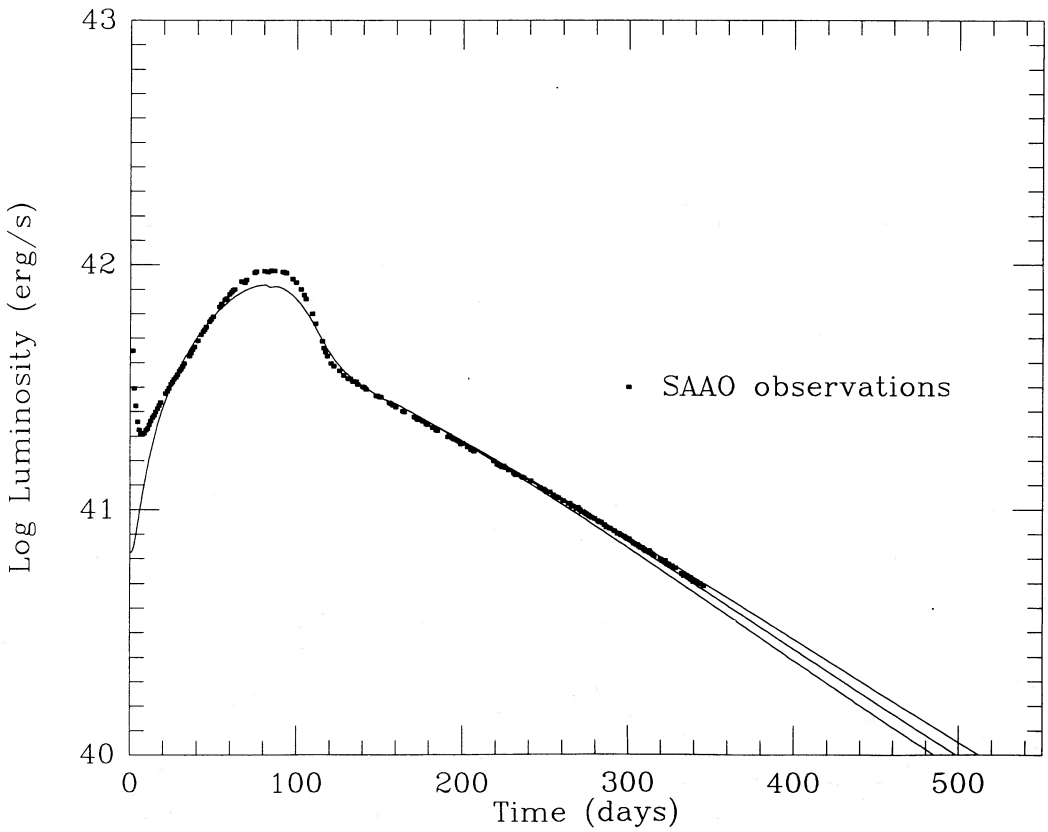

FIG. 6.—Bolometric light curve for an ejected mass of 7.5 $M_\odot$, with a density increase toward the center. The notation is the same as for Fig. 2. The standard case (uniform density) is shown for comparison; it is the lowest curve. For the middle curve, the density varies as $\rho \propto \exp(-x)$; for the higher curve, the dependence is $\rho \propto \exp(-2x)$. Only the "sag" in the exponential tail is sensitive to these changes; the gamma-ray attenuation involves the density distribution in an exponential function while thermal diffusion does not. The behavior of the light curve after 120 days probes the innermost regions of the supernova ejecta.

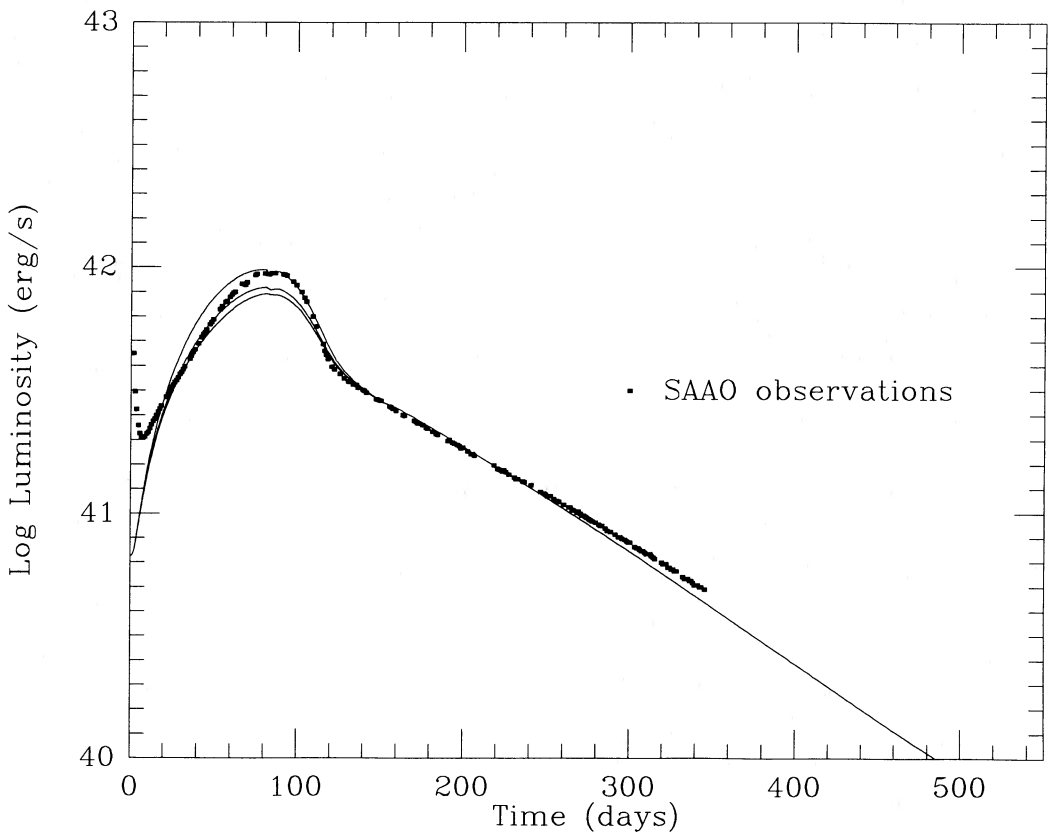

FIG. 7.—Bolometric light curve for an ejected mass of 7.5 $M_{\odot}$, with different ionization energies. The notation is the same as for Fig. 2. The standard case (33.6 eV) is shown for comparison; it is the middle curve. The lower curve corresponds to an average ionization energy of 11.6 eV per nucleon and the upper curve to 100 eV per nucleon.

a) The Effect of Changes in Mixing Radius

Bolometric and gamma-line light curves for an ejected mass of 15 $M_{\odot}$, for different choices of mixing radius b, are shown in Figure 8. The detections for the 0.847 MeV gamma-ray line from the *Solar Maximum Mission* (*SMM*) (Matz *et al.* 1987, 1988), Lockheed-Marshall (LM) (Sandie *et al.* 1988), CIT (Cook *et al.* 1988), and the GRAD (Rester *et al.* 1988) experiments imply rates of energy loss by escape of superthermal photons which are shown. The theoretical luminosities for the gamma-ray escape are plotted as dashed curves. The data for other gamma-ray lines were not plotted in order to avoid confusion in the figure; they are quantitatively similar, within the quoted errors. The higher dashed curve corresponds to mixing of ^{56}Co out to a fractional radius $b = 0.4$, while the lower curves correspond to $b = 0.2$ and 0.1, respectively. The time of emergence of the gamma rays is later than observed, although not by so much as other theoretical estimates (compare Woosley, Pinto, and Ensman 1988; Gehrels, MacCallum, and Leventhal 1987, Ebisuzaki and Shibazaki 1987; Chan and Lingenfelter 1987 to Arnett 1988*a*). Using their parameters, we have explicitly recalculated all the cases considered by Gehrels *et al.* (1987) and several considered by Woosley *et al.* (1988). The agreement for timing and flux of the maximum gamma-ray line luminosity is good. The essential differences seem to be the treatment of mixing as a hydrodynamic process, the underlying presupernova model, and the explosion mechanism. These differences probably represent a reasonable measure of the theoretical uncertainty at present.

Because the gamma-ray line detections are all close to the minimum detectable signal, we attempt to infer a corresponding gamma-ray line flux from the *Ginga* data. The *Ginga* flux by number on September 3 is ~ 1.5 times that of *SMM*, which was 10^{-3} cm^{-2} s^{-1}. At the earliest detection (late June), the number flux seen was lower than the September 3 value by a factor of 6. If the gamma rays are downscattered to X-ray energies by Compton scattering, their number is conserved. First detection is expected when the number of scatters to the surface equals the number of scatters needed to get to the energy of the K-edge for absorption. In § II we estimated this to be ~ 60 scatters, which corresponds to an optical depth of 8 or so for the X-rays. We scale this by the ratio of the gamma-ray attenuation cross section (Klein-Nishina) to X-ray scattering cross section (Thomson), so the attenuation length for gamma-rays is ~ 2.7. With these assumptions, we infer a luminosity for escaping gamma rays of $\log L_{\rm infer} \approx 37.7 \pm 0.7$ in cgs units. This value is shown as a crossed box in Figure 8. We use this simple estimate to illustrate the constraint, and note that it is consistent with the general shape of the theoretical light curves for gamma-ray lines.

b) The Effect of Increasing Central Density

Bolometric and gamma-ray line light curves for an injected mass of 7.5 $M_{\odot}$, for different choices of density structure, are shown in Figure 9. In all cases, mixing of ^{56}Co out to a fractional radius $b = 0.4$ was assumed. These density variations are the same as those used previously in Figure 6. The gamma-

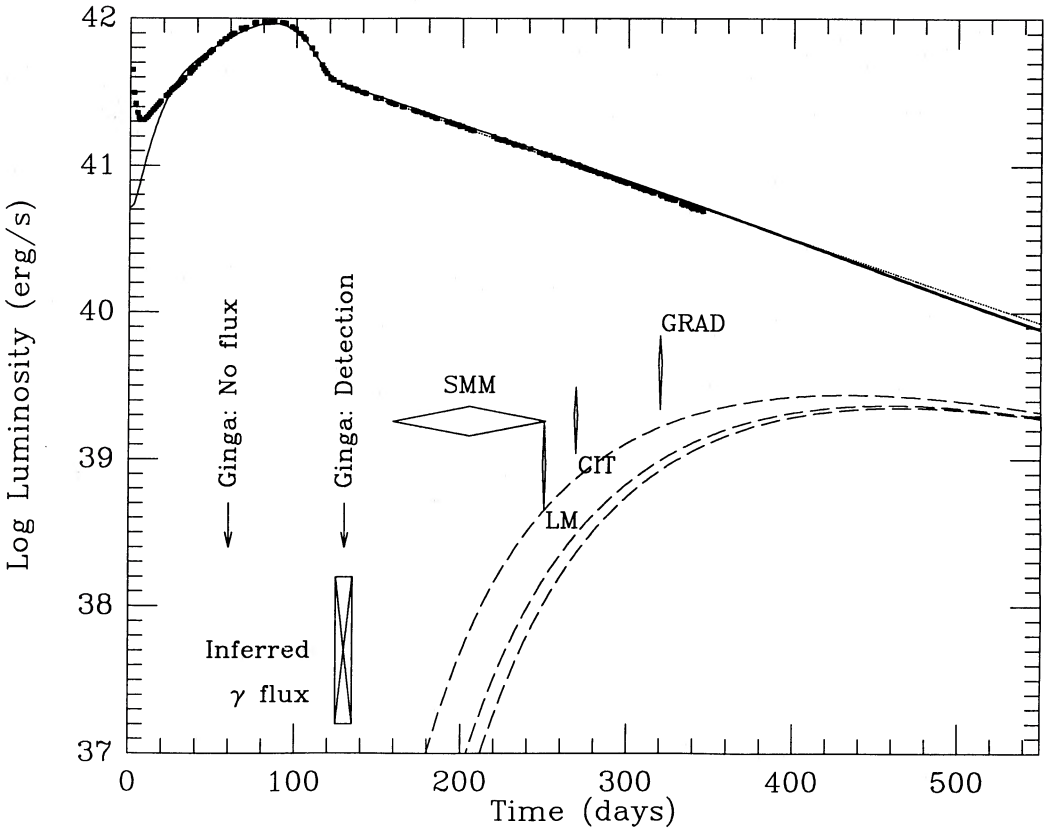

FIG. 8.—Bolometric and gamma-ray line light curves for an ejected mass of 15 $M_\odot$, for different choices of mixing radius b. The detections for the gamma-ray lines from the *Solar Maximum Mission*, Lockheed-Marshall, Caltech, and the GRAD experiments are shown. A value inferred from the *Ginga* X-ray detection is shown as a crossed box (see text for details). The theoretical luminosities for the gamma-ray lines are plotted as dashed curves. The higher dashed curve corresponds to mixing of ^{56}Co out to a fractional radius $b = 0.4$, while the lower curves correspond to $b = 0.2$ and 0.1, respectively. The time of emergence of the gamma-rays is overestimated.

ray luminosities implied by the detections for the 0.847 MeV gamma-ray line from the *SMM* (Matz *et al.* 1987, 1988), LM (Sandie *et al.* 1988), CIT (Cook *et al.* 1988) and the GRAD (Rester *et al.* 1988) experiments are shown. The theoretical luminosities for the gamma-ray lines are plotted as dashed curves.

The uniform density case gives a line luminosity which exceeds the observational data. It also has an unacceptable sag in its thermal light curve. The intermediate case—for which increasing density toward the center reduces gamma-ray escape–reproduces the thermal light curve better, but lies below the *Ginga* and *SMM* and above the LM and CIT points. There is a bit too much sag to match the SAAO light curve well. The lowest curve fits the light curve better but lies below the *Ginga* and *SMM* points, as did the 15 $M_\odot$ case above.

The combination of the early detection by *Ginga* and *SMM* and the closely exponential light curve by SAAO constrain the possible distribution of ^{56}Co. The early detection requires some ^{56}Co to be almost unattenuated, while the exponential decline requires that most ^{56}Co be buried. The sag in the optical light curve must correspond to the light curves in X-rays and gamma rays. Unfolding this behavior will give us the distribution of ^{56}Co in the supernova.

The attenuation length for gamma rays can be changed by moving material nearer the surface or by clearing voids so that we can see in deeper. These cases may be distinguished by observations of Doppler shifts of the matter; improved data on gamma-ray line shapes is needed. An interesting alternative may be developed from infrared lines (Rank *et al.* 1988).

c) *The Effect of* ^{56}Co *Bubbles*

Figure 10 shows the behavior of the gamma-ray light curve for a distribution of ^{56}Co having some small amount of material at low attenuation depths. The lowest dashed curve is the standard case for the 15 $M_\odot$. The curve that rises first corresponds to the standard case, but with a fraction 0.01 of the ^{56}Co uniformly mixed to $b = 0.9$ as well. The highest curve corresponds to the standard case, but with a fraction 0.1 of the ^{56}Co uniformly mixed to $b = 0.8$ as well. Our attenuation algorithm is not accurate for such large radii, so that only the qualitative behavior should be considered. These second ^{56}Co bubbles correspond to high velocities, low-density holes, or both. It seems plausible that many distributions can be found that fit the data. A proper treatment of this "inverse problem" would include X-ray spectra, and gamma-ray and optical line shapes and shifts as well, so that some of the extra possibilities can be eliminated.

V. PULSAR HEATING

While the neutrino detection suggests the formation of a neutron star as strongly as 19 counts can, we are ignorant as to whether a pulsar has yet begun to operate. The strongly exponential nature of the postpeak light curve constrains the pos-

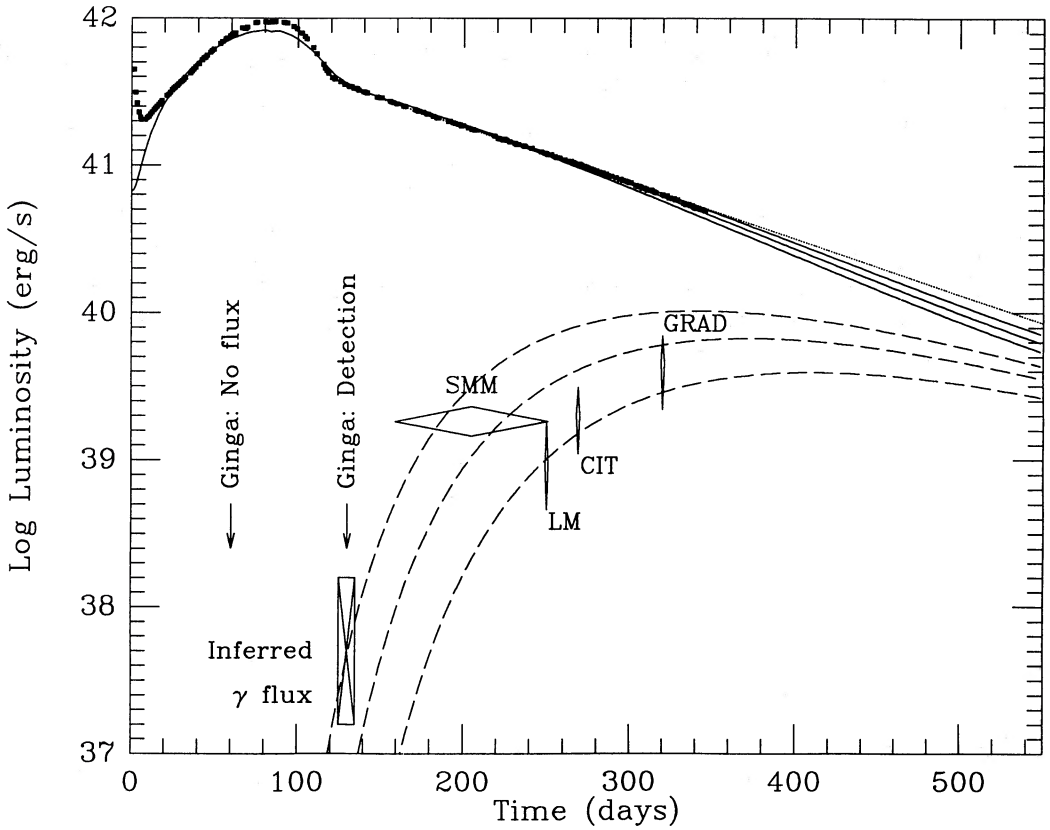

FIG. 9.—Bolometric and gamma-ray line light curves for an ejected mass of 7.5 $M_\odot$, for different choices of density structure. The density variations are the same as for Fig. 6, and the notation the same as Fig. 8. In all cases, mixing of ^{56}Co out to a fractional radius $b = 0.4$ was assumed. The theoretical luminosities for the gamma-ray lines are plotted as dashed curves. The higher dashed curve corresponds to uniform density, while the lower curves correspond to the density variations used previously in Fig. 6. Note that for correct tracking of the exponential tail of the light curve, the predicted time of emergence of the gamma-ray is overestimated, as was the case in Fig. 8.

sible energy input to the expanding ejecta (Arnett 1988*a*; see also Michel, Kennel, and Fowler 1987; Woosley 1989).

Suppose the pulsar luminosity is trapped by the expanding ejecta. For times of order 300 days after core collapse, the pulsar luminosity is thought to be slowly varying (Ostriker and Gunn 1969). Figure 11 illustrates the effect of such a pulsar luminosity on the light curve for SN 1987A. In this case the gamma-ray line emission is unaffected (by assumption). The top curve represents the addition of a pulsar luminosity of $L_{\rm pulsar} = 5 \times 10^{39}$ ergs s^{-1}; it diverges from the SAAO data after 300 days. The second curve corresponds to $L_{\rm pulsar} = 2 \times 10^{39}$ ergs s^{-1}, which is the largest value consistent with the data at present. The lowest curve is also consistent with the data and corresponds to $L_{\rm pulsar} = 1 \times 10^{38}$ ergs s^{-1}; smaller values give equivalent light curves at this epoch. For comparison we note that the Ostriker and Gunn (1969) model gave $L_{\rm pulsar} \approx 10^{42}$ ergs s^{-1} at 1 yr for electromagnetic luminosity.

If the Crab pulsar has a total luminosity of $L_{\rm pulsar} \approx 5 \times 10^{38}$ ergs s^{-1} now and this scales as the angular velocity to the fourth power, then we estimate that the pulsar in SN 1987A must have a period $P \geq 0.023$ s, if the magnetic fields are assumed to be comparable. The simplest interpretation is that the neutron star was formed by slowly rotating, a view consistent with the agreement of the electron-type antineutrino burst with predictions of core collapse dynamics which ignored rotational effects.

Figure 12 gives an expanded view of the thermal luminosity from SN 1987A, for the same pulsar luminosities as in Figure 11. The deviation of the top curve is obvious. It appears that the thermal curve is beginning to sag due to gamma-ray escape. Contemporaneous observations in optical, X-ray, and γ-ray bands are vital for understanding this epoch.

Figure 13 shows the later evolution of the light curves. The top curve is the upper limit of $L_{\rm pulsar} = 2 \times 10^{39}$ ergs s^{-1}, the middle curve is $L_{\rm pulsar} = 1 \times 10^{38}$ ergs s^{-1}, and the bottom curve is for no pulsar luminosity. The gamma-ray light curve is the same for all three cases. The continuing decrease in thermal luminosity makes it comparable to other luminosities which might be relevant. Two examples are illustrated. The Eddington luminosity for a 1.5 $M_\odot$ neutron star is shown; this might be important if there is significant fallback of nearly ejected matter. For matter spherically expanding at about one-third of the speed of light into a medium of density of one nucleon cm^{-3} the "swept-up" luminosity after 1 yr is $\sim 3 \times 10^{39}$ ergs s^{-1}. Because this depends strongly upon the conditions assumed, the particular number is to be considered as a fiducial value, for illustrative purposes. It is important to look for indications of luminosity from new processes, especially in the X-ray region.

The pulsar problem is not a simple one, but significant progress has been made in recent years (see Ruderman 1986; Kennel and Coroniti 1984). If the MHD outflow from the pulsar is largely positronic, we expect that a significant fraction of the flux into the ejecta will be in the form of gamma rays. As

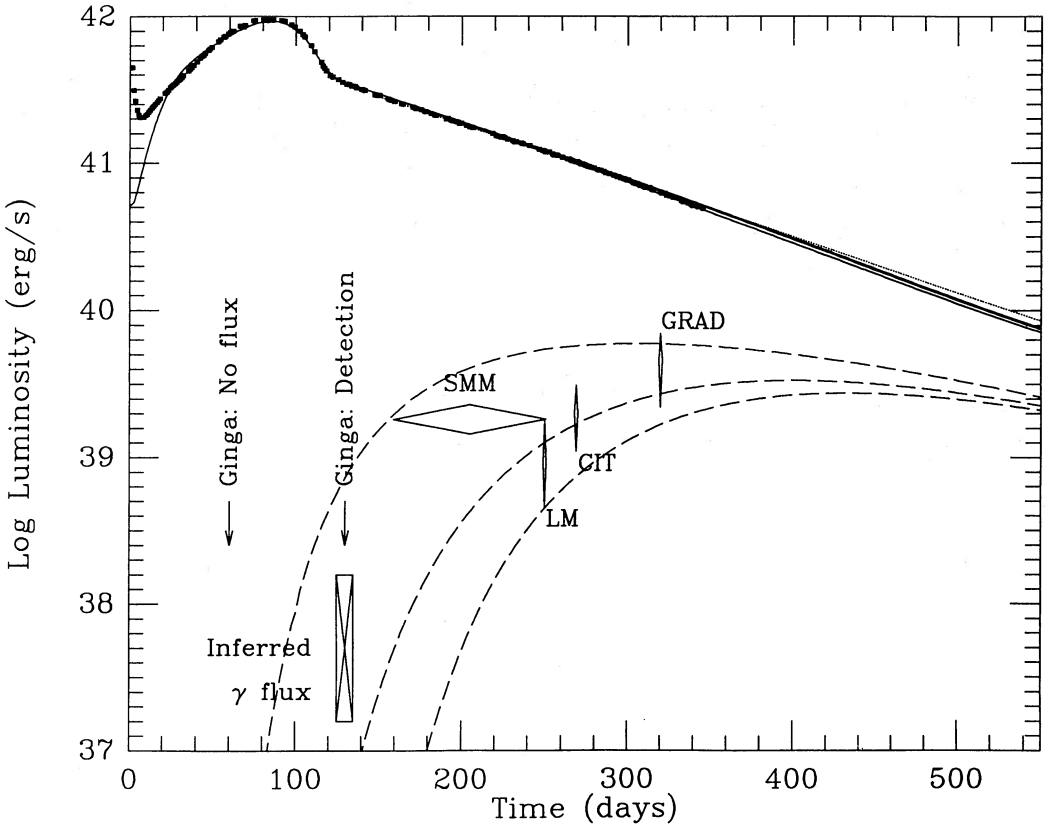

FIG. 10.—Bolometric and gamma-ray line light curves for an ejected mass of 15 $M_\odot$, for different choices of ^{56}Co distribution. The notation is the same as for Fig. 8. In all cases, most of the ^{56}Co was mixed out to a fractional radius $b = 0.4$. The lowest dashed curve is the standard case for the 15 $M_\odot$. The curve that rises first corresponds to the standard case, but with a fraction 0.01 of the ^{56}Co uniformly mixed to $b = 0.9$ as well. The highest curve corresponds to the standard case, but with a fraction 0.1 of the ^{56}Co uniformly mixed to $b = 0.8$ as well. Our attenuation algorithm is not accurate for such large radii, so that only the qualitative behavior should be considered.

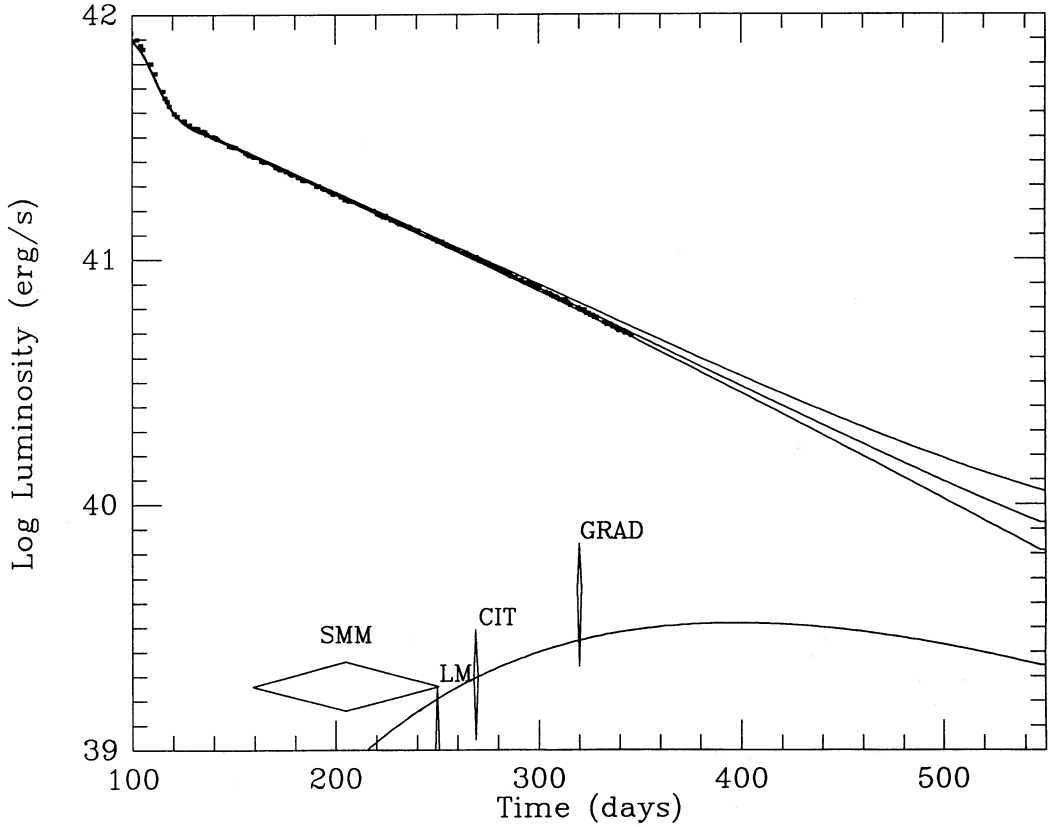

FIG. 11.—Bolometric and gamma-ray line light curves for an ejected mass of 15 $M_\odot$, for different choices of pulsar luminosity. The notation is the same as for Fig. 8. Top curve represents the addition of a pulsar luminosity of $L_{\rm Pulsar} = 5 \times 10^{39}$ ergs s^{-1}; it diverges from the SAAO data after 250 days. The second curve corresponds to $L_{\rm pulsar} = 2 \times 10^{39}$ ergs s^{-1}, which is the largest value consistent with the data at present. The lowest curve is also consistent with the data and corresponds to $L_{\rm pulsar} = 1 \times 10^{38}$ ergs s^{-1}; smaller values give equivalent light curves at this epoch. The gamma-ray luminosity is the same for the three cases.

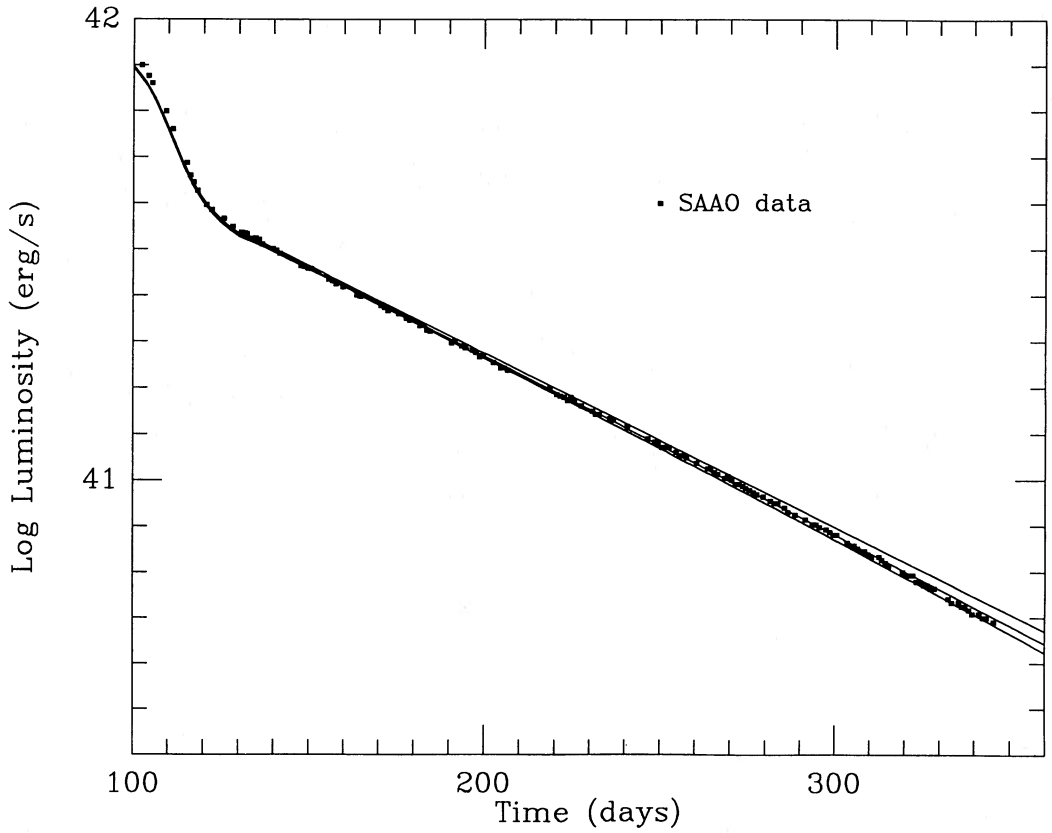

FIG. 12.—Bolometric light curves for an ejected mass of 15 $M_\odot$, for different choices of pulsar luminosity, shown in detail. The notation is the same as for Fig. 11. Top curve represents the addition of a pulsar luminosity of $L_{\rm pulsar} = 5 \times 10^{39}$ ergs s^{-1}; it diverges from the SAAO data after 250 days. The second curve corresponds to $L_{\rm pulsar} = 2 \times 10^{39}$ ergs s^{-1}, which is the largest value consistent with the data at present. The lowest curve is also consistent with the data and corresponds to $L_{\rm pulsar} = 1 \times 10^{38}$ ergs s^{-1}; smaller values give equivalent light curves at this epoch. The sag is becoming evident after 300 days.

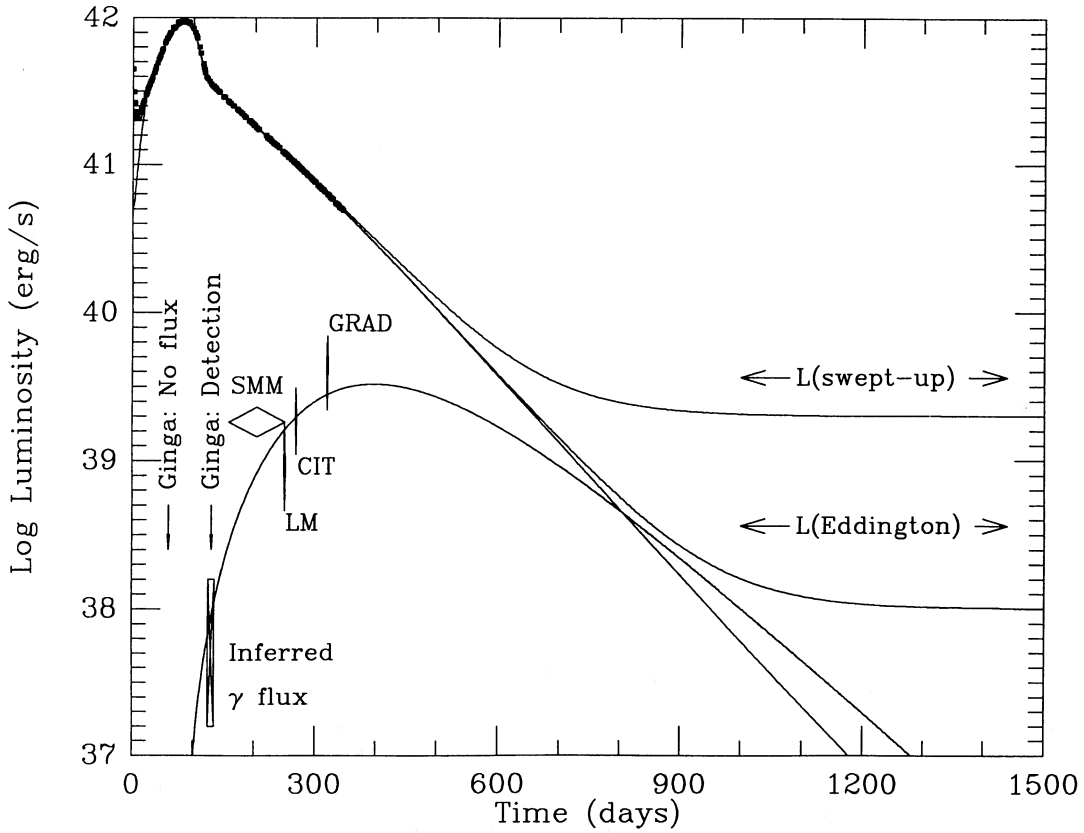

FIG. 13.—Bolometric light curves for an ejected mass of 15 $M_\odot$, for different choices of pulsar luminosity, for still later times. The notation is the same as for Fig. 11. Top curve represents the addition of a pulsar luminosity of $L_{\rm pulsar} = 2 \times 10^{39}$ ergs s^{-1}. The second curve corresponds to $L_{\rm pulsar} = 1 \times 10^{38}$ ergs s^{-1}. The lowest curve corresponds to $L_{\rm pulsar} = 0$. Luminosity from circumstellar matter L(sweptup) and accretion L(Eddington) are shown (see text). Notice the dramatic effect of an embedded pulsar on later luminosity.

a first step, let us suppose that the pulsar luminosity is in the form of gamma radiation, and for simplicity take the mean energy of these photons to be 0.847 MeV, the same as the dominant line from the ^{56}Co decay. We assume the gamma rays to be injected at the center of the ejected mass and treat their attenuation as described above for the ^{56}Co lines.

Figure 14 shows the effect of this different treatment of pulsar luminosity. The curves correspond to the same parameters as in Figure 11. The thermal light curves are nearly unchanged, but additional gamma-ray flux is expected from the higher pulsar luminosities. Our tentative conclusion that the neutron star is slowly rotating is unaffected.

At later times this different model of the pulsar has testable implications, as Figure 15 illustrates. In particular, if the pulsar is radiating at our upper limit, its gamma-ray luminosity is constant to within a factor of 2 or 3 for the first 3 years after core collapse. At that time essentially all the gamma rays of energies around 1 MeV escape the ejecta and, for this luminosity, could be detected with instruments which have already flown. Unfortunately this presumes a particular spectrum of gamma-ray energies from the pulsar; a careful investigation of this point is needed.

If the abundance ratio of newly synthesized Ni^{57} to Ni^{56} is similar to the solar system ratio of the corresponding Fe isotopes, as calculations of explosive nucleosynthesis have been predicting for almost two decades, then the heating of the Ni^{57} to Co^{57} to Fe^{57} will not be comparable to that of the Ni^{56} chain until $\sim$1114 days (3.05 yr), when the 391 day mean lifetime of Co^{57} begins to compensate for its smaller gamma-ray energy and lower abundance. The lower energy of the Co^{57} gamma rays inhibits their escape relative to those produced by Co^{56}, or (possibly) those expected from the pulsar. This late decay mimics a pulsar of $L \approx 10^{38}$ ergs s^{-1}, and is almost a factor of 10 less than the Eddington luminosity for a neutron star of 1.5 $M_\odot$ (see Fig. 13).

VI. CONCLUSIONS

The analytic light curves provide a powerful tool for analyzing SN 1987A; these results may be compared to the numerical work of Pinto and Woosley (1988) and Itoh *et al.* (1987). We find that the observational data are most naturally explained for an ejected mass which lies in the range $15 \geq M/M_\odot \geq 7.5$, with the larger values favored.

The presence of 0.073 ± 0.015 $M_\odot$ of freshly synthesized ^{56}Ni is needed to fit the bolometric light curve; the error estimate is dominated by uncertainty in the distance to the supernova. This matter must be well distributed in attenuation depth in the ejecta, as could be the case if the Rayleigh-Taylor instability encountered in Arnett (1987, 1988*a*) were operative, and/or clumping in density occurred. This modifies the light curve and predictions of X-ray and γ-ray escape. The γ-ray line flux is sensitive to the density and position of the radioactive matter; this may provide a constraint on the nature of the explosion.

The accurately exponential decay of the bolometric light

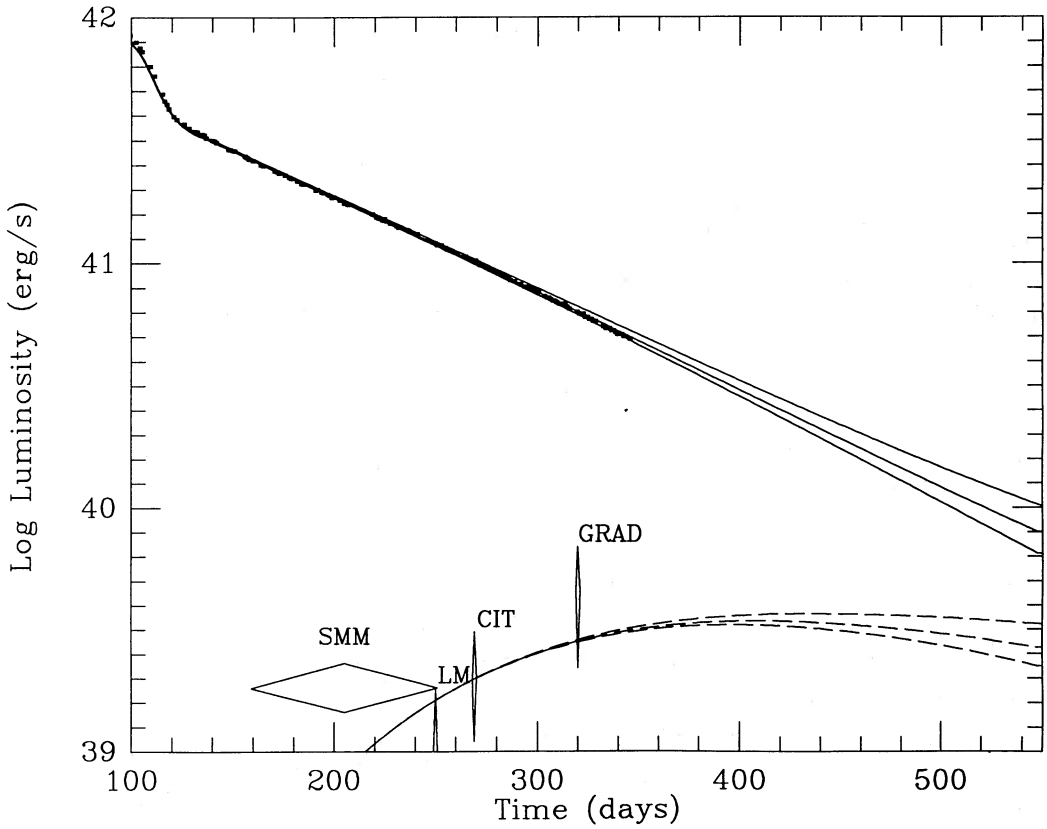

FIG. 14.—Bolometric light curves for an ejected mass of 15 $M_\odot$, for different choices of pulsar luminosity, assuming that luminosity is dominated by gamma-ray radiation. The parameters are the same as for Fig. 11; the only change is the possibility of gamma-ray escape from the pulsar. Top curve represents the addition of a pulsar luminosity of $L_{pulsar} = 5 \times 10^{39}$ ergs s^{-1}; it still diverges from the SAAO data after 250 days. The second curve corresponds to $L_{pulsar} = 2 \times 10^{39}$ ergs s^{-1}; the lowest curve corresponds to $L_{pulsar} = 1 \times 10^{38}$ ergs s^{-1}. These show little change from Fig. 11. The gamma-ray luminosity is larger for the larger pulsar luminosities.

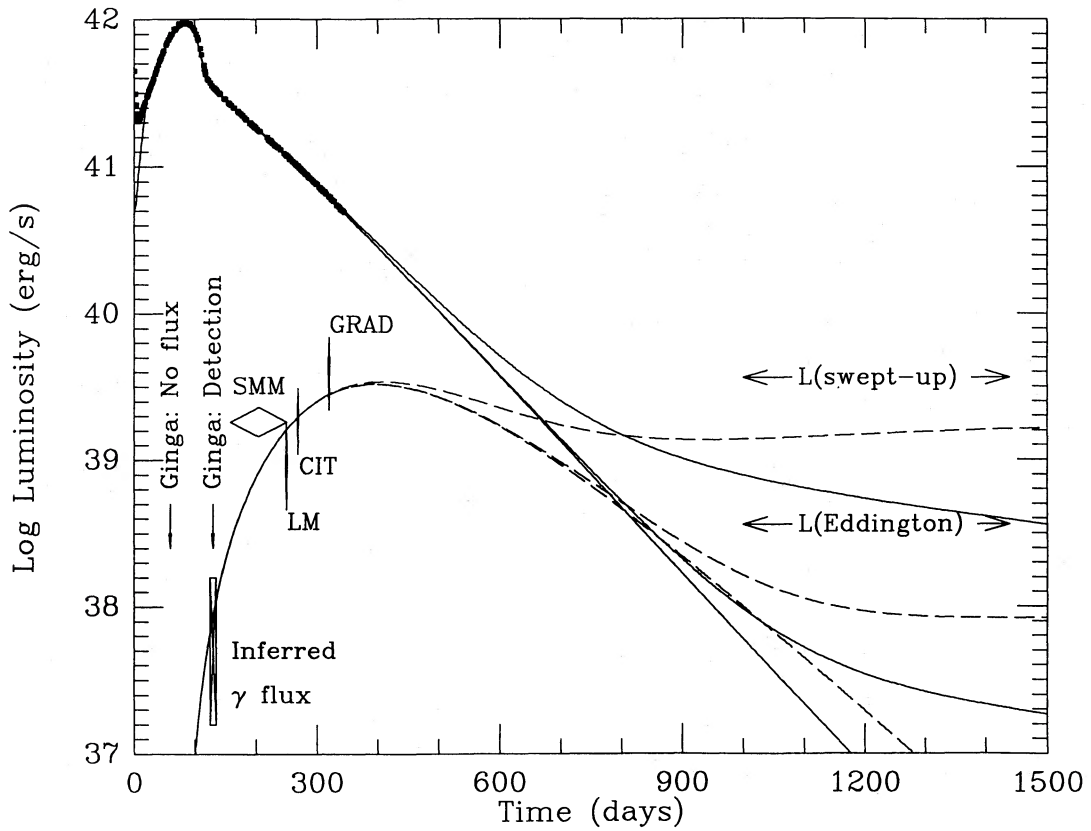

FIG. 15.—Bolometric light curves for an ejected mass of 15 $M_\odot$, for different choices of pulsar luminosity, assuming that luminosity is dominated by gamma radiation. The parameters are the same as for Fig. 13; the only change is the possibility of gamma-ray escape from the pulsar. Top curve represents the addition of a pulsar luminosity of $L_{\rm pulsar} = 2 \times 10^{39}$ ergs s^{-1}. The second curve corresponds to $L_{\rm pulsar} = 1 \times 10^{38}$ ergs s^{-1}. The lowest curve corresponds to $L_{\rm pulsar} = 0$. Luminosity from circumstellar matter L(sweptup) and accretion L(Eddington) are shown (see text). The effect of an embedded pulsar on later luminosity is more subdued than in Fig. 13, but still dramatic. The gamma-ray luminosity for the $L_{\rm pulsar} = 2 \times 10^{39}$ ergs s^{-1} case (*top dashed curve*) is almost steady from 300 to 1500 days.

curve for $t > 120$ days places severe limits on the luminosity ($L \leq 2 \times 10^{39}$ ergs s^{-1}) and the presumed period ($P \geq 2 \times 10^{-2}$ s) of the newly formed pulsar/neutron star. Such an object might make itself known shortly by its effect on the thermal light curve or by its gamma-ray emission.

The authors wish to acknowledge helpful conversations with many colleagues, and especially A. Burrows, D. Q. Lamb, C. Michel, and G. Share. Particular thanks are due to Robin Catchpole and his colleagues at SAAO for providing their beautiful data prior to publication.

APPENDIX

In order to include the effects of ionization and to obtain a form more convenient for use on personal computers, we rederive the approximate solutions for supernova light curves (Arnett 1980, 1982; hereafter A80 and A82). The notation follows these two papers.

I. THE DIFFERENTIAL EQUATIONS

The first law of thermodynamics may be written for a spherical star as

$$dE/dt + P\,dV/dt = \epsilon - (1/\rho r^2)\partial(r^2 F)/\partial t\,, \tag{A1}$$

where

$$F = -(\lambda c/3)\partial(aT^4)/\partial r\,, \tag{A2}$$

and the symbols have their usual meanings.

For a homologous expansion, the radius r may be separated into time and Lagrangian space-dependent factors,

$$r = xR(t)\,, \tag{A3}$$

and the fluid velocity scales as $v(r, t) = x\,dR/dt$, where

$$dR/dt = v_{\rm sc}\,. \tag{A4}$$

Here the variable x is a dimensionless radius. We define the useful variables $\eta(x)$, $\phi(x)$, and $\psi(x)$ by

$$\rho(r, t) = \rho(0, 0)\eta(x)R(0)^3/R(t)^3 , \tag{A5}$$

and

$$T(r, t)^4 = T(0, 0)^4\psi(x)\phi(t)R(0)^4/R(t)^4 . \tag{A6}$$

Similarly, the energy generation rate ϵ and the opacity κ may be written as

$$\epsilon(r, t) = \epsilon(0, 0)\xi(x)\zeta(t) , \tag{A7}$$

and

$$\kappa(r, t) = \kappa_t \theta(T - T_{\rm ion}) . \tag{A8}$$

Here is the step function (unity for positive arguments, zero otherwise). This crude approximation is reasonably good for Rosseland mean opacities for matter at the low densities appropriate to this problem.

If the heating rate ϵ is due to the decay of ^{56}Ni and the ^{56}Co, the abundances by mass fraction obey

$$dX(\mathrm{Ni})/dt = -X(\mathrm{Ni})/\tau(\mathrm{Ni}) , \tag{A9}$$

$$dX(\mathrm{Co})/dt = +X(\mathrm{Ni})/\tau(\mathrm{Ni}) - X(\mathrm{Co})/\tau(\mathrm{Co}) , \tag{A10}$$

and the dimensionless heating function is

$$\zeta(t) = \{X(\mathrm{Ni}) + X(\mathrm{Co})[\epsilon(\mathrm{Co})/\epsilon(\mathrm{Ni})]\}D(t) , \tag{A11}$$

where

$$\epsilon(\mathrm{Ni}) = Q(\mathrm{Ni})/\tau(\mathrm{Ni}) , \tag{A12}$$

$$\epsilon(\mathrm{Co}) = Q(\mathrm{Co})/\tau(\mathrm{Co}) , \tag{A13}$$

and we normalize the $\zeta(t)$ by choosing $\epsilon(0, 0) = \epsilon(\mathrm{Ni})$. Here τ denotes the mean lifetime for decay and Q is the energy released by the decay of a unit mass of the radioactive nucleus. The deposition function $D(t)$ accounts for escape of gamma rays from the object before they deposit energy (see A82, § IV*a*).

II. THE CASE OF NO RECOMBINATION

For temperatures above the ionization temperature $T_{\rm ion}$, the previous results remain valid, and the following nondimensional ordinary differential equations are obtained:

$$d\phi/dz = \sigma(z)[p_1\zeta(z) - p_2\,\phi(z)] , \tag{A15}$$

$$d\sigma/dz = p_3 , \tag{A15}$$

$$dX(\mathrm{Ni})/dz = -X(\mathrm{Ni}) , \tag{A16}$$

and

$$dX(\mathrm{Co})/dz = +X(\mathrm{Ni}) - p_4\,X(\mathrm{Co}) , \tag{A17}$$

where $z \equiv t/\tau(\mathrm{Ni})$ is a slightly different variable than used in A82 and

$$\zeta(z) = X(\mathrm{Ni}) + p_5\,X(\mathrm{Co}) , \tag{A18}$$

$$\sigma(z) \equiv R(t)/R(0) , \tag{A19}$$

with

$$p_1 \equiv \tau(\mathrm{Ni})\epsilon(\mathrm{Ni})M_{\rm Ni}(0)/E_{\rm th}(0) , \tag{A20}$$

$$p_2 \equiv \tau(\mathrm{Ni})/\tau(d) , \tag{A21}$$

$$p_3 \equiv \tau(\mathrm{Ni})/\tau(h) , \tag{A22}$$

$$p_4 \equiv \tau(\mathrm{Ni})/\tau(\mathrm{Co}) , \tag{A23}$$

$$p_5 \equiv \epsilon(\mathrm{Co})/\epsilon(\mathrm{Ni}) . \tag{A24}$$

The mass of newly synthesized ^{56}Ni (at time $t = 0$) is

$$M_{\rm Ni}(0) = 4\pi R(0)^3\epsilon(0, 0)\rho(0, 0)\int_0^1 \xi(x)\eta(x)x^2\,dx ; \tag{A25}$$

we will denote this dimensionless integral as $I_{\rm Ni}$. The total thermal energy at time $t = 0$ is

$$E_{\rm th}(0) = 4\pi R(0)^3 aT(0, 0)^4\int_0^1 \phi(x)x^2\,dx ; \tag{A26}$$

this dimensionless integral is denoted $I_{\rm th}$. The time scale for hydrodynamic expansion is

$$\tau(h) \equiv R(0)/v_{\rm sc}\,, \tag{A27}$$

and that for radiative diffusion is

$$\tau(d) \equiv 3\rho(0,\,0)\kappa_t R(0)^2 I_{\rm th}/c\,. \tag{A28}$$

This is identical with equation (10) of A82 if we use the identity $I_{\rm th} = 1/\alpha$, where α is the separation parameter which acts as the eigenvalue for the solution of the spatial equation (see A80):

$$\alpha = -(1/x^2\phi)\partial[(x^2/\eta)\partial\phi/\partial x]/\partial x\,. \tag{A29}$$

For a given solution of equation (A25) with eigenvalue α, equations (A13)–(A16) may be solved by standard techniques (e.g., Runga-Kutta integration) to obtain the light curve for a given set of parameters p_i. As shown previously (A82), the luminosity is

$$L(1,\,t) = E_{\rm th}\,\phi(z)/\tau(d)\,. \tag{A30}$$

For example, the tabulated light curve function of Table 1 in A82 may be calculated in this way (note that the Λ function tabulated there is related to $\phi(z)$ by eq. [36] of that paper).

III. THE CASE OF RECOMBINATION

In order to develop an approximate solution which includes the effects of recombination (i.e., opacity defined by eq. [A8] above rather than simply constant), we use a more accurate version of the approach in Arnett (1979). We will integrate (1) over the Lagrangian spatial variable x, and approximate the spatial solution (eq. [A25]) by a radiative zero solution from the central temperature down to the ionization temperature $T_{\rm ion}$. This will occur at a dimensionless radius x_i. If we define the total internal energy to be

$$E^* \equiv \int_0^{R(i)} aT^4 4\pi r^2\,dr\,, \tag{A31}$$

then, assuming shape invariance of $\phi(x)$,

$$\int_0^{x_i} \phi(x)x^2\,dx = x_i^3 \int_0^1 \phi(x)x^2\,dx\,, \tag{A32}$$

we have

$$E^* = [aT(0,\,0)^4 4\pi R(0)^3][\phi(t)/\sigma(t)]x_i^3\,I_{\rm th}\,. \tag{A33}$$

This differs from the previous case only by the factor x_i^3 which corrects the total energy for the smaller volume inside the photosphere. Direct differentiation gives

$$dE^*/dt = E^*[d\ln(\phi)/dt - d\ln(R)/dt + 3d\ln(x_i)/dt]\,, \tag{A34}$$

and similar integration over the $P\,dV/dt$ term gives

$$dE^*/dt + (P\,dV/dt)^* = E^*[d\ln(\phi)/dt + 3d\ln(x_i/dt]\,, \tag{A35}$$

where we have used

$$d\ln(V)/dt = 3d\ln(R)/dt\,, \tag{A36}$$

and equations (A3), (A4), and (A5).

Integration over the heating term gives

$$\epsilon^* = [4\pi R(0)^3\rho(0,\,0)\epsilon(0,\,0)\zeta(t)\int_0^1 \xi(x)\eta(x)x^2\,dx\,, \tag{A37}$$

where the dimensionless integral is denoted $I_{\rm Ni}$. We have explicitly assumed that the radioactive matter is concentrated toward the center and that the $D(t)$ factor in equation (11) accounts for all loss of radioactive heating. This is a choice of convenience; alternatively we could have modified the upper limit of integration as above, but then we would have to add explicitly a contribution from the nebula (the region above the photosphere) to the luminosity, and calculate the nature of the nebula with a radioactive source of heat. While important to the details, we do not expect these choices to make a qualitative difference here.

The total mass is given by

$$M = 4\pi R(0)^3\rho(0,\,0)\int_0^1 \eta(x)x^2\,dx\,, \tag{A38}$$

where the dimensionless integral is I_M.

The integral of the diffusion term in equation (1) gives the luminosity evaluated at the upper limit of integration. If we use

$$d\psi(x)dx = -1/x_i \tag{A39}$$

at $x = x_i$, we then find

$$L(1, 0) = 4\pi[acT(0, 0)^4/3\rho(0, 0)\kappa_t]\phi(t)[x_i/\eta(x_i)] . \quad \text{(A40)}$$

After some algebra, we may combine these results to obtain

$$d\phi/dz = (\sigma/x_i^3)[p_1\zeta - p_2\phi - 2(\phi/\sigma)x_i^2\, d(x_i)/dz] , \quad \text{(A41)}$$

and

$$L(1, 0) = x_i E_{\rm th}(0)\phi(z)/\tau(d) . \quad \text{(A42)}$$

In equation (A37) we have a factor of $1/x_i^3$ and a new term in $d(x_i)/dz$, relative to our previous result (eq. [A13]). Similarly equation (A38) has a new factor of x_i relative to equation (A26).

It remains to evaluate x_i and its time derivative. The procedure is to choose a solution of equation (A25) for $\psi(x)$. Note that as the recombination wave recedes inward in x, the eigenvalue α increases as $1/x_i^2$ from scaling. Then $\psi(x_i)$ is determined by setting $T = T_{\rm ion}$ and using equation (A6). Now invert $\psi(x_i)$ to get x_i. If the function ψ is analytic, the time derivative of x_i may be obtained by direct differentiation; otherwise finite difference approximations may be necessary. Note that for uniform density ($\eta = 1$), $\psi(x) = \sin(\pi x)/\pi x \approx 1 - x^2$ gives a qualitatively correct behavior and is simple to invert.

Finally, we note that as the recombination wave moves inward through the matter, it releases as energy Q per unit mass recombined. The total luminosity is $L_{\rm total} = L(1, 0) + L_{\rm ion}$, where

$$L_{\rm ion} = 4\pi r^2 \rho Q\, dr_i/dt , \quad \text{(A43)}$$

where dr_i/dt is the velocity with which the recombination wave moves *inward* through the matter. This is essentially the same as the speed with which the photosphere moves inward through the matter. For pure hydrogen, $Q = 13.6$ eV per proton $\approx 1.36 \times 10^{13}$ ergs g^{-1}. For larger Z, the situation is more complex. While the Thomas-Fermi model of the atom gives a total binding energy of

$$Q \approx 16Z^{7/3} \text{ eV per atom} , \quad \text{(A44)}$$

or

$$Q \approx 1.6 \times 10^{13}(Z/A)Z^{4/3} \text{ ergs g}^{-1} \quad \text{(A45)}$$

(see Landau and Lifshitz 1965, p. 244), this recombination energy is released over a range of different temperatures, and therefore in different parts of the star. Note that 1 $M_\odot$ of ^{16}O recombining would release 2.5×10^{47} ergs; over 10^7 s this would have an average energy release of 2.5×10^{40} ergs s^{-1}, which is about one-sixth that of SN 1987A at that age. The recombination of 10 $M_\odot$ of hydrogen-rich matter would give a similar energy release. It appears that recombination energy is important but is probably not dominant for this supernova.

REFERENCES

Arnett, W. D. 1979, *Ap. J.* (*Letters*), **230**, L37.
———. 1980, *Ap. J.*, **237**, 541.
———. 1982, *Ap. J.*, **253**, 785.
———. 1987, *Ap. J.*, **319**, 136.
———. 1988*a* in *Supernova 1987A in the Large Magellanic Cloud: Proc. of the Fourth George Mason Astrophysics Workshop*, ed. M. Kafatos and A. G. Michalitsianos (Cambridge: Cambridge University Press), p. 301.
———. 1988*b*, *Ap. J.*, **331**, 337.
Bionata, R. M., *et al.* 1987, *Phys. Rev. Letters*, **58**, 1494.
Catchpole, R. M., *et al.* 1988, *M.N.R.A.S.*, **229**, 15P.
Chan, K. W., and Lingenfelter, R. E. 1987, *Ap. J.* (*Letters*), **318**, L51.
Colgate, S. A., Petscheck, A. G., and Kriese, J. T. 1980, *Ap. J.* (*Letters*), **237**, L81.
Cook, W. R., Palmer, D., Prince, T., Schindler, S., Starr, C., and Stone, F. 1988, *IAU Circ.*, No. 4527.
Dopita, M. A. 1988, *Nature*, **331**, 506.
Dotani, T., *et al.* 1987, *Nature*, **330**, 230.
Ebisuzaki, T., and Shibazaki, N. 1988, *Ap. J.* (*Letters*), **327**, L5.
Elias, J. H., and Gregory, S. C. 1989, in preparation.
Falk, S. W., and Arnett, W. D. 1973, *Ap. J.* (*Letters*), **180**, L65.
Fu, A., and Arnett, W. D. 1989, *Ap. J.*, **340**, 414.
Gehrels, N., MacCallum, C. J., and Leventhal, M. 1987, *Ap. J.* (*Letters*) **320**, L19.
Hirata, K. 1987, *Phys. Rev. Letters*, **58**, 1490.
Itoh, M., Kumagai, S., Shigeyama, T., Nomoto, K., and Nishimura, J. 1987, *Nature*, **330**, 233.
Kennel, C. F., and Coroniti, F. V. 1984, *Ap. J.*, **283**, 694.
Landau, L. D., and Lifshitz, E. M. 1965, *Quantum Mechanics* (Oxford: Pergamon).
Lucy, L. 1988, in *Proc. 4th George Mason Astrophysics Workshop, Supernova 1987A in the Large Magellanic Cloud*, ed. Kafatos and A. G. Michalitsianos (Cambridge: Cambridge University Press), p. 323.
Matz, S. M., Share, G. H., Leising, M. D., Chupp, E. L., Vestrand, W. T., Purcell, W. R., Strickman, M. S., and Reppin, C. 1988, *Nature*, **331**, 416.
Menzies, J. W., *et al.* 1987, *M.N.R.A.S.*, **227**, 39P.
Michel, F. C., Kennel, C. F., and Fowler, W. A. 1987, *Science*, **238**, 938.
Nomoto, K., Shigeyama, T., and Hashimoto, M. 1987, in *Proc. ESO Workshop on the SN 1987A*, ed. I. J. Danziger (Munich: European Southern Observatory), p. 325.
Ostriker, J. P., and Gunn, J. E. 1969, *Ap. J.*, **157**, 1395.
Pinto, P. A., and Woosley, S. E. 1988, *Ap. J.*, **329**, 820.
Rank, D. M., Pinto, P. A., Woosley, S. E., Bregman, J. D., Witteborn, F. C., Axelrod, T. S., and Cohen, M. 1988, *Nature*, **331**, 505.
Rester, A. C., Eichhorn, G., and Coldwell, R. L. 1988, *IAU Circ.*, No. 4526.
Ruderman, M. 1986, in *Cosmogonical Processes*, ed. W. D. Arnett, C. J. Hansen, J. W. Truran, and S. Tsuruta (Utrecht: NU Science Press), p. 199.
Sandie, W., Nakano, G., and Chase, L. 1988, *IAU Circ.*, No. 4526.
Sunyaev, R., *et al.* 1987, *Nature*, **330**, 227.
Woosley, S. E. 1989, in preparation.
Woosley, S. E., Pinto, P. A., and Ensman, L. 1988, *Ap. J.*, **324**, 466.

W. David Arnett: Department of Physics, University of Arizona, Tucson, AZ 85721

Albert Fu: Department of Physics, Northwestern University, Evanston, IL

THE ASTROPHYSICAL JOURNAL, 340:414–425, 1989 May 1

THE LATE BEHAVIOR OF SUPERNOVA 1987A. II. GAMMA-RAY TRANSPARENCY OF THE EJECTA

ALBERT FU
Northwestern University, Department of Physics and Astronomy
AND
W. DAVID ARNETT
Department of Astronomy, Physics, and the Enrico Fermi Institute, University of Chicago
Received 1988 April 4; accepted 1988 June 23

ABSTRACT

In the wake of news of gamma rays detected by the *SMM* satellite from SN 1987A, and continued reports of X-rays detected by *Ginga*, we investigate the problem of computing the luminosities in gamma-ray lines and in X-rays from the supernova, employing results of (1) radiation hydrodynamic models for the bolometric light curve (Arnett 1987), and (2) analytic light curve models (Arnett and Fu 1989), in order to constrain several parameters which are crucial for calculation of the radiative transfer. In addition, these results point to two important uncertainties: (1) the extent of mixing of NiCo–rich matter in the ejecta, and (2) the mass density profile during the coasting phase of the expansion. By exploring a range of both the radioactive mass distribution and density profile, we find that the high-energy observations strongly suggest the development of large-scale clumping and "bubbling" of radioactive material in the ejecta. The favored models have a hydrogen envelope mass of $\sim 7\ M_\odot$, homologous scale expansion velocities of ~ 3000 km s^{-1}, and an approximately uniform mass distribution. As we show, these features are consistent with three important constraints: (1) the presupernova mass had a helium core of $6\ M_\odot$; (2) the edge of the helium core is moving at ~ 2100 km s^{-1}; (3) values of E_{SN}/M are constrained by the early optical observations and models to be $0.7(\pm 0.3) \times 10^{17}$ ergs g^{-1}.

Subject headings: gamma rays: general — nucleosynthesis — stars: individual (SN 1987A) — stars: supernovae — X-rays: sources

I. INTRODUCTION

Stellar evolution theory and radiative hydrodynamics have been used with marked success to explain the early behavior of SN 1987A with regard to timing of the neutrino burst and shock breakout, evolution of the total luminosity, and evolution of important spectral features (see, for instance, Arnett 1987, hereafter Paper I; Woosley, Pinto, and Ensman 1988; Lucy 1987). Computational simulations, however, have encountered difficulty in reproducing the bolometric light curve after ~ 20 days, when the radiative emission from the supernova was, and has been through the present, controlled by radioactive decay of NiCo. However, the analytic models of Arnett (1980, 1982), suitably enhanced to include the dynamic effects of a recombination wave, have emerged as the one class of models to date which are capable of achieving agreement with the observed postpeak behavior of the bolometric light curve (Arnett and Fu 1989; hereafter Paper II). Indeed, a reasonably accurate treatment of the ionization balance in the ejecta, along with the inclusion of time-dependent nonspherical motions, are precisely the main physical ingredients missing from the computational models. Calculations of this magnitude will require more effort.

Currently, the emission of X-rays and gamma-ray lines from the supernova are topics of prime importance. Anticipation of detectable fluxes reprocessed from nuclear gamma-rays down to X-ray and UV wavelengths provided motivation for preliminary studies (see, e.g., McCray, Shull, and Sutherland 1987; Fransson and Chevalier 1987). The actual detection of X-rays from SN 1987A in the 10–30 keV band by the *Ginga* satellite (Makino 1987*a*, *b*, *c*; Dotani *et al.* 1987) was followed by several theoretical studies of the gamma-ray radiative transfer in the ejecta (Pinto and Woosley 1988; Gehrels, McCallum, and Leventhal 1987; Ebisuzaki and Shibazaki 1988; Chan and Lingenfelter 1987). Most of these studies have employed the structure and evolution of numerical light curve models in order to calculate X-ray and gamma-ray spectra and light curves via Monte Carlo methods and approximate integrations of the transfer equation. Diverse results exist because of varying choices of underlying model. The recent report of the detection of 847 keV gamma-ray lines by the *Solar Maximum Mission* (*SMM*) satellite (Matz *et al.* 1988), roughly *coincident* with the *Ginga* X-ray detection, has clearly shown the need for further calculation. Since the detected 847 keV flux was extremely high ($\sim 1.1 \times 10^{-3}$ cm^{-2} s^{-1}) and early (~ 6 months after the explosion) by most anticipated estimates, one might immediately postulate the existence of a very extended distribution of radioactive material (Itoh *et al.* 1987). This is perhaps supported by the *SMM* detection of the 1238 keV flux (Matz *et al.* 1988) at a level roughly consistent with the relevant branching ratio in the $Co^{56} \rightarrow Fe^{56}$ decay chain, suggesting that the emitting material was nearly "bare." Indeed, the observed flux is equivalent to complete uncovering of $\sim 1\%$ of the total mass of Ni^{56} synthesized in the explosion, a level consistent with the persistent traversal of the optical light down its "$0.075\ M_\odot$ exponential track" until recently (Catchpole and Whitelock 1988). In such a scenario one faces the problem of justifying the existence of high-lying parcels of NiCo and finding their spatial distribution. On the other hand, it might be possible to uncover material located at depth initially (say, inside the edge of the helium core) at the required

early times if the scale expansion velocity is high enough and/or the column density above the radioactive source is low enough by virtue of a tenuous mass distribution at larger radii.

In an effort to address these difficulties, we shall examine in this paper some effects which strongly influence the time scales, intensities, and shapes of the gamma-ray and X-ray light curves, all within the context of the radioactive heating and emission scenario. At the same time, we shall use the combined results of Papers I and II as judiciously as possible to constrain the set of parameters which we vary. We also complete the analytic model outlined in Paper II by finding under what conditions the analytic treatment of gamma transparency outlined therein is valid. In § II, we discuss the relevant set of parameters for our study and the corresponding models. In § III, we describe the various methods of our approximation to the gamma-ray radiative transfer. In § IV, we present the results and discuss which models might be significant in light of the current high-energy observations. Conclusions are presented in § V.

II. PARAMETERS OF THE MODELS

In the following, we consider models of equal complexity to the analytic models of Paper II to characterize the temporal and spatial dependence of the medium through which gamma rays are transferred (as for the radiative transfer itself, we shall employ methods outlined in § III). Thus we employ a linear, homologous velocity profile with scale velocity v_{sc}, and a homologous density profile $\eta(x)$, where $x = r/R$ and R is the instantaneous SN radius. All calculations shall have a 6 $M_\odot$ helium core (Woosley *et al.* 1987; Woosley, Pinto, and Ensman 1988; Paper I) overlaid by a hydrogen envelope. We shall consider (1) "bulk" radioactive sources extended to the edge of the helium core, i.e., $x_{Ni} = x_{He}$ (designated as *b* in Paper II), (2) highly extended "clumped" sources with NiCo located well beyond the edge of the He core. For simplicity, radioactive sources shall be "clumped" by distributing the material in discrete shells or bands. The total amount of Ni^{56} in all calculations shall be 0.075 $M_\odot$.

However, in this paper two crucial parameters, M, the total ejected mass, and v_{sc}, shall be constrained in a different manner than in Paper II. There the values of M and v_{sc} were chosen primarily from the detailed numerical results of Paper I. Alternatively, here we simply fit a linear velocity profile to three constraints: (1) the range of values of E_{SN}/M inferred from the early light curve and more precisely fitted by the models of Paper I, (2) the core of the presupernova star of 6 $M_\odot$ (Woosley *et al.* 1987), and (3) the motion of the edge of the helium core at $\sim$2100 km s^{-1} Details of this procedure are described below shortly. This method is favorable because it makes use of the second and third constraints in a straightforward way, yet it suffers from an overstringency of the assumption of homology and linearity of the velocity profile. Hence, we stress that this approach yields a fairly well defined range of the parameters M and v_{sc}, although it does not suggest any one particular pair of these parameters within this range. Indeed, this is sufficient for the present work, for it seems clear from the results presented below that the pivotal feature responsible for the detected emergence of hard X-rays and gamma rays is the distribution of NiCo in the ejecta. Until further observational and theoretical progress concerning the kinematics and structure of the radioactive material within the supernova can be made, it would seem premature to attempt to constrain the envelope mass and velocities more closely than attempted here.

a) Escape Probability and Optical Depth

The features of the gamma-ray light curve depend on x_{Ni}, v_{sc}, the total mass M, composition, and $\eta(x)$, via the escape probability $e^{-\tau}$, hence the optical depth τ. The sensitivity of the onset of transparency to these parameters is conveniently shown by considering the outward radial optical depth τ_R of the fastest moving NiCo. It is easy to show that

$$\tau_R = \frac{\sigma_{KN} N_0 M Y_e}{4\pi(vt)^2}\left(\frac{\phi}{I_2}\right), \tag{1}$$

where

$$\phi = \int_{x_N}^{1} \eta(x)dx$$

is the dimensionless column density, and

$$I_2 = \int_0^1 x^2\eta(x)dx,$$

$\sigma_{KN}(v)$ is the Klein-Nishina cross section of gamma rays of frequency v, and Y_e is the number of electrons per nucleon. This expression is strongly dependent on the velocity v_{sc} but is independent of $R(0)$, since only at late times, for which $vt \gg R(0)$, does τ_R become small enough to allow gamma rays to escape. An especially informative case is uniform density, $\eta(x) = 1$, for which the above expression becomes

$$\tau_R = \frac{3\sigma_{KN} N_0 M Y_e(1 - x_{Ni})}{4\pi(vt)^2}. \tag{2}$$

Here we can see that τ_R varies significantly with x_{Ni} (per decade) only for $x_{Ni} \gtrsim 0.1$; hence all models in which $x_{Ni} \lesssim 0.1$ (with other parameters kept fixed) should yield the same gamma ray light curve. This is indeed verified by the detailed calculations presented below.

b) Density, Velocity, Total Mass, and Composition

The success in reproducing the later optical light (Paper II) by using, in part, crude analytic approximations to the detailed structure of the numerical models of the early evolution (Paper I) suggest that these approximations are not a gross misrepresentation of the actual supernova. This is especially noteworthy if we consider the changes in velocity, composition, and density structure which undoubtedly occurred during the development of Rayleigh-Taylor instabilities as a result of radioactive heating (Falk and Arnett 1973; Woosley *et al.* 1987). Thus we can assert that Papers I and II together provide a combination of ingredients for a viable model of the gamma-ray transfer, although by no means a complete combination. These works yield estimates of $\eta(x)$, v_{sc}, Y_e, and M. Let us discuss each of these in turn.

i) *Homologous Density Profile, $\eta(x)$*

The complicated density variation in Paper I is approximated by uniform density, $\eta(x) = 1$. As discussed in Paper II, the density declines by only a factor of $\sim$100 over $\sim$99% of its mass before plunging in a steep power law in the nonhomologous outer layers. Attempting to fit the density variation present in the early numerical models with more complicated profiles would necessarily imply deeper assumptions of the thermal evolution of the optical model, since this would invoke higher order modes of solution to the analytic light curve, expressed as $T(x, t)$ for a given $\eta(x)$. This higher order behavior, discussed in the context of Type II supernovae in Arnett (1980),

is well beyond the scope of this paper, and of Paper II. However, because of the uncertainty in the profile modified by mixing, and in order to explore the combined effects of central condensation of the mass distribution and extent of the NiCo, we shall also consider an extremely centrally condensed profile which nevertheless preserves the mild density contrast of ~ 100 over most of the envelope mass. For definiteness, we consider $\eta(x) = 0.99 \exp(-ax^2) + 0.01$, which preserves the density contrast for large values of a. In an ongoing investigation of the sensitivity of the SN evolution to the inner boundary condition of the explosion, Arnett (1988) obtains a mass distribution qualitatively similar to this one when the entropy of the innermost zones (i.e., the partitioning of the shock energy between internal and kinetic) is more closely related to the actual physics of the core collapse than has previously been calculated.

ii) *Scale Velocity, v_{sc}*

Here we are referring to the velocity at the edge of the homologous mass M. As explained in Arnett (1982) and shown in Paper II, the immediate postshock behavior of the optical light curve of an event like SN 1987A is determined largely by the shock deposited energy per unit mass E_{SN}/M and the initial radius $R(0)$. The initial release of thermal energy depends on E_{SN} divided by the initial diffusion time $t_0 \approx M\kappa/[R(0)c]$; hence, the initial "plateau" luminosity (~ 4 days after the neutrino burst; see Sonneborn and Kirshner 1987) depends on $(E_{SN}/M)R(0)$. The timing of the neutrino burst with the initial optical data constrains $R(0)/(E_{SN}/M)$. Therefore, the early data provide estimates of $R(0)$ and E_{SN}/M which have been made quantitative through the computational studies of Paper I; the values $R(0) = 3(\pm 1) \times 10^{12}$ cm and $E_{SN}/M = 0.7(\pm 0.3) \times 10^{17}$ ergs g^{-1}, as noted in that work, are required to fit the early observations. Since E_{SN} is approximately twice the initial kinetic energy of the ejecta, the specific energy E_{SN}/M can be related to v_{sc}^2 via the density distribution. This yields $v_{sc}^2 = (I_2/I_4)(E_{SN}/M)$, which for $a = 0$ gives $v_{sc} \cong (2.5\text{–}4.0) \times 10^8$ cm s^{-1}.

iii) *Homologous Mass, M*

Although a negligible amount of column mass is nonhomologous, the real uncertainty here is the total mass when the star explodes, i.e., the mass of the hydrogen envelope. One straightforward way to obtain an estimate of M hinges on the analytic estimate of $\eta(x)$, and takes advantage of two particularly stiff constraints. The first is observational: spectroscopic data on infrared hydrogen lines and also of Fe II (Phillips *et al.* 1988; Elias and Gregory 1989), as pointed out by Pinto and Woosley (1988), show that the edge of the helium core is moving at ~ 2100 km s^{-1}. The second is theoretical: the presupernova star, regardless of its present envelope mass, had a ~ 6 $M_\odot$ helium core when it exploded (Woosley *et al.* 1987; Woosley, Pinto, and Ensman 1988; Paper I). Thus, from the range of v_{sc} as given above, we have the range of radial extent of the helium core directly (since $v_{He}/v_{sc} = x_{He}$): $0.52 \leq x_{He} \leq 0.84$ for $a = 0$. Now, once, again, making use of $\eta(x)$, we obtain the corresponding mass fraction,

$$\frac{M_{He}}{M} = \frac{\int_0^{x_{He}} x^2 \eta(x) dx}{\int_0^1 x^2 \eta(x) dx} = \frac{I_{2x}}{I_2}, \tag{3}$$

where here it should be stressed that $M_{He} \approx 4.5$ $M_\odot$ because the innermost ~ 1.5 $M_\odot$ settles to form the neutron star. The range of mass thus obtained for $a = 0$ is $8.36 \leq M \leq 33.1$ $M_\odot$. Obviously, we will disregard the upper end of this range.

iv) *Composition, Y_e*

Here, by employing the radiative transfer methods outlined below, it is easy to include explicitly the inhomogeneity of a helium core with an outer hydrogen envelope, in contrast to the analytic optical models, in which a mass-weighted average Y_e is employed for the entire star. We also note that in considering the consequences of Rayleigh-Taylor mixing of the NiCo in the ejecta, we do not consider the mixing of other heavy elements in the manner of Shigeyama *et al.* (1987) and Shull and Xu (1987), which can have, as these authors show, significant effects on the hard X-ray light curve.

c) *Combined Effects of the Parameters on the Gamma-ray Transparency*

It is worth remarking on the possibile combined effects of M, v_{sc}, and x_{He} on the gamma-ray transparency when these quantities are determined in the manner described above. For our calculations, we have $x_{Ni} \approx x_{He} = v_{He}/v_{sc}$, whereby the dependence of t_R on M, v_{sc}, and x_{Ni} becomes, making use of equation (3),

$$\tau_R \propto \left(\frac{M}{v_{sc}^2}\right)\left(\frac{\phi}{I_2}\right) = \left(\frac{M_{He}}{v_{sc}^2}\right)\left(\frac{\phi}{I_{2x}}\right), \tag{4}$$

that is, τ_R depends only on $\eta(x)$ and v_{sc}. We note the circumstance whereby the *column mass above x_{He} is actually increased by increasing v_{sc}*—because v_{sc} determines x_{He}, increasing v_{sc} increases the radial fraction above the edge of the helium core; consequently, for a fixed $\eta(x)$, this lessened x_{He} corresponds to a smaller mass fraction, which, for the fixed value of M_{He}, gives a larger total mass M. Indeed, it can easily be shown that as v_{sc} increases from 2500 to 4000 km s^{-1} (the preferred range for $a = 0$), τ_R *increases* by a factor of ~ 4, showing that the increased column mass overwhelms the v_{sc}^2 dependence in the optical depth. Thus in Figure 1 we plot τ/τ^0 versus v_{sc} for $\eta(x) = 0.99 \exp(-ax^2) + 0.01$, for $a = 0$, 3, 6, 9, 12, where, from equation (4), $\tau/\tau^0 = (v_{sc}^{02}/v_{sc}^2)(\phi/\phi^0)(I_{2x}^0/I_{2x})$, and the superscript corresponds to the lower limit value of v_{sc} for $a = 0$. Each line segment corresponds to a distinct value of a, the preferred range of v_{sc} being determined by $\eta(x)$ and the uncertainty in E_{SN}/M (Paper I). As a increases, the extent of the helium core recedes in x for a fixed value of E_{SN}/M because of the increasing central condensation of the mass distribution. Because its edge moves at 2100 km s^{-1}, this results in higher scale velocities. Also because of the tenuous tail of the density profile, lower total masses result. These lower masses and higher velocities (i.e., lower densities) give significantly more optically thin media than the uniform density case—in the range $a \approx 10$–12, as shown in Figure 1, the hydrogen envelope would be ~ 3–4 times as transparent at any given time as one which has uniform density.

Again, we stress that it is not our intention to "zero in" on any particular values of M and v_{sc}, although our procedure *logically* gives pairs of values of these parameters for a given E_{SN}/M. Consider the case $a = 0$. The main information to be gained is that the constraints used, along with the assumption of a linear velocity profile, yield (1) a moderate range of v_{sc} of ~ 2500–4000 km s^{-1}, with a corresponding wider range in M of 8.36–33.1 $M_\odot$, and (2) preferentially low values v_{sc} (~ 2500–3000 km s^{-1}), since they are associated with reasonable values

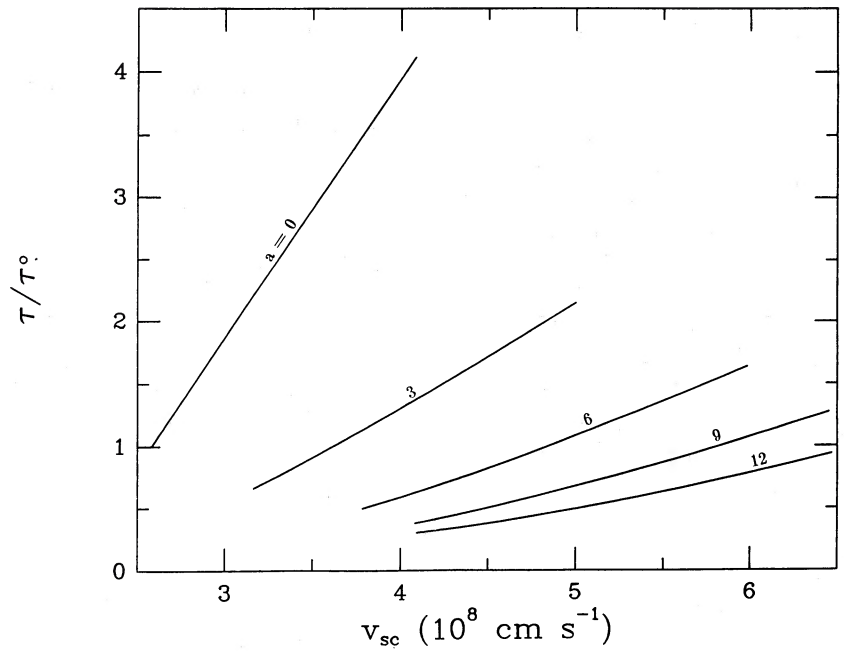

FIG. 1.—Plots of τ/τ^0, the mass and velocity dependence of the optical depth, as explained in the text, for the density profile $\eta(x) = 0.99 \exp(-ax^2) + 0.01$. Each curve corresponds to a particular value of a as noted, and the cases $a = 0$, 3, 6, 9, and 12 are shown. The limits for each curve are determined by the range of E_m/M allowed by the calculations of Paper I.

of M (less than $\sim 15\ M_\odot$). Thus the "allowed" models by this procedure should not be strictly confined, for instance, to the points on the line segments shown in Figure 1.

From the above discussion, it is plausible to consider three models which are summarized in Table 1.

The mass which characterizes models UBB and UEC was chosen partially on the basis of the models considered in Paper II, which have ejected envelopes of 7.5 and 15 $M_\odot$. Here we consider an intermediate mass of 11.15 $M_\odot$, nearly halfway in between these two values. The pair of values for M and v_{sc} corresponded, in an older set of calculations, to the most transparent model for uniform density and an *ejected helium core of* 6 $M_\odot$. A similar model is also "allowed" by the revised calculations which have an ejected helium core of 4.5 $M_\odot$, although for 11.15 $M_\odot$ the velocity is slightly higher (~ 2800 km s^{-1}). The exact choice, however, is secondary, for a simple analytic calculation of the 847 keV luminosity from a *bulk source* in a model with $M = 8.36\ M_\odot$ and $v_{sc} = 2580$ km s^{-1} (i.e., the most transparent model for $a = 0$ in the revised set) reveals the inability of these parameters to achieve the required level of flux (by a few orders of magnitude) at the approximate gamma-ray turn-on time (160 days). *Therefore, we cannot justify any particular choice of the parameters M and v_{sc} on the basis of the gamma-ray light curve alone without allowing for the possibility of very extensive mixing of the radioactive matter.* Hence, we consider two opposite extreme cases of NiCo, namely, (1) placing 1% of the radioactive mass in a shell at the surface (UBB), and (2) distributing the entire radioactive mass in clumps all the way out to the surface of the ejecta (UEC).

In retrospect, and as seen in Figures 2, 3, and 6 (to be discussed shortly), the values of M and v_{sc} chosen were found to yield an excellent set of results. Also, model UBB will give a ratio of 1238 keV to 847 keV flux equal to the 0.68 branching ratio at the required early time, consistent with the *SMM* determination of this flux ratio as 0.6 ± 0.25, whereas UEC will give a higher gamma-ray flux at later times. Model NUB has a significantly lower mass and a higher velocity by virtue of its mass distribution, and is thus capable of releasing gamma rays from a bulk source much earlier than the uniform density models; from Figure 1 we see that it is ~ 3 times more transparent than the most transparent uniform density model. Such a case is presented as a possibility of reproducing the high-energy observations without having to invoke large-scale "bubbling" of the NiCo beyond the edge of the He core.

III. RADIATIVE TRANSFER METHODS

For an extended NiCo distribution, we have found that the most efficient method of calculating the gamma-ray light curve utilizes random numbers to choose random emission angles of individual rays, and subsequently accumulates an emergent

TABLE 1

MODEL PARAMETERS

Model	Mass ($M_\odot$)	v_{sc} (km s^{-1})	Density Profile ($\eta(x)$)	NiCo Distribution
UBB	11.15	2580	Uniform	Bulk($x_{Ni} = x_{He}$) + band at $x = 1$
UEC	11.15	2580	Uniform	Extended, clumps out to $x = 1$
NUB	8.49	4108	$0.99 \exp(-10x^2) + 0.01$	Bulk($x_{Ni} = x_{He}$)

flux by exponential attenuation of each ray out to the continuously expanding surface of the ejecta. Such a procedure sacrifices little in computing expense when compared to solutions of the transfer equation, since the scattering process is not followed in detail and small photon samples can be used (in our case, each model emitted 5000 photons per day of evolution, which required ~ 0.25 s of CPU time to tabulate as emergent flux on an ELXSI 6400 computer). In addition, the code is much simpler to construct, treats the time dependence of the evolution exactly (although not strictly necessary—typical photon flight times are $\sim R/c$, which is much smaller than the hydrodynamic time, R/v_{sc}), and does not suffer from inaccuracies due to approximations of the forward peaking of the radiation field in a spherical medium (variable Eddington factors, flux limiting).

The validity of this method hinges on the large average frequency shift of a gamma ray upon Compton scattering. The diffuse component of the radiation field contributes negligibly to the gamma-ray line flux, which emerges as prompt photons along their original directions of emission and at a level determined by the escape probability $e^{-\tau}$. Therefore, exponential attenuation along each ray of emission determines this flux quite precisely.

Nevertheless, we have employed two other related transfer methods for other distinct purposes:

1. *Analytic.*—Here, as pointed out in Paper II, the radioactive source emits photons only radially, with half emitted inward, half outward. In this approximation, it is easy to integrate over an extended source to obtain the total gamma-ray luminosity for a given epoch of the evolution. This has been outlined in detail in Paper II; here, we investigate the accuracy of this simplified treatment for calculation of the emergent gamma-line flux by considering different values of x_{Ni} for a uniform density medium and fixed values of M and v_{sc}.

2. *Full Monte Carlo simulation.*—Here we calculate the Comptonization of gamma-ray lines down to the hard X-ray regime (20–30 keV), utilizing probability distributions and their associated random variables to represent the detailed scattering process. This seems to have been the method of choice for calculating the spectral flux in X-rays and gamma rays; here, we use it to calculate the light curve in the 20–30 keV range and the spectrum of Comptonized gamma rays down to 20 keV for comparison with the *Ginga* observations as summarized in Dotani *et al.* (1987).

IV. RESULTS AND DISCUSSION

a) Gamma-Ray Light Curves

Figure 2 shows how the current gamma-ray observations for the 847 keV line can be bracketed by models UBB and UEC. The mild dip in the UBB light curve at ~ 300 days is the point at which the bulk source starts to dominate the emergent flux; these features keep the flux at a more or less constant level for several hundred days. Because of the greater mass of NiCo located above the helium core in model UEC, this light curve achieves a much higher maximum than UBB, consistent with the tentative estimate of the GRAD detection (Rester *et al.* 1988). Both light curves come close to matching the initial detection at ~ 160 days by the *SMM* satellite (Matz *et al.* 1987).

The "effervescent" behavior of the supernova is probably dynamic, so the actual light curve may fluctuate somewhere in between UBB and UEC. For instance, if the first substantial Co "bubble" ($\sim 1\%$ of the NiCo mass) rises and becomes transparent at ~ 160 days, the emergent flux will rapidly rise at this time to $\sim 10^{-3}$ cm^{-2} s^{-1}, and may then decline for a short period, following the behavior of model UBB; subsequent emergence of other Co bubbles might cause fairly abrupt rises in luminosity, so that the situation at later times might resemble the clump distribution exemplified in UEC. As we shall see

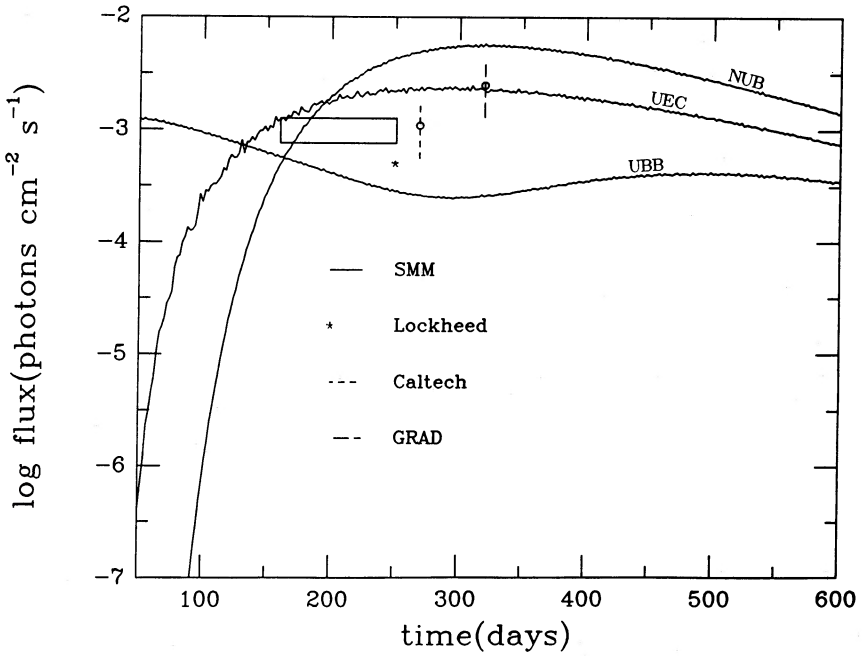

FIG. 2.—847 keV light curves for models UBB, UEC, and NUB. Points are tentative estimates to the gamma-ray line flux determined by the observers as noted, including error bars wherever possible.

below, the X-ray observations suggest a slightly modified picture. Of course, because of the uncertainties involved in the analysis of the gamma-ray detections, observations are also not inconsistent with a roughly constant level of flux from ~ 150 days up to the present.

Figure 2 also shows that the initial *SMM* detection can be fit by model NUB. However, because of its significantly enhanced transparency over the uniform density models with bulk sources, the emergent flux continues to rise to a level even higher than model UEC. Indeed, this behavior cannot be avoided—in order to fit the early emergence of gamma rays (as detected by *SMM*) without large-scale clumping, the light curve at this epoch must be at the onset of gamma transparency, and must therefore be undergoing a rapid rise. This leads to an extremely high and broad flux maximum extending over several hundred days. Such high levels of luminosity are unlikely, since they imply a premature sag in the *optical* light (Paper II) which was not observed. (Indeed, the 7.5 $M_\odot$ model considered in Paper II has nearly the same column depth to the fastest moving NiCo as model NUB.) Therefore, we must consider this model to be an unlikely possibility for now. A modified scenario combining a more centrally condensed radioactive source with $x_{\rm Ni} < x_{\rm He}$, a small amount of NiCo in high lying clumps, and a centrally condensed mass distribution like that in NUB will produce a light curve similar to UBB, but at a higher level to achieve a closer fit to the tentative observations. Future observations and current two- and three-dimensional calculations of hydrodynamic mixing in the ejecta (Fryxell and Arnett 1988) should clarify this situation considerably.

b) *X-Ray Light Curves*

In Figure 3 are shown the X-ray light curves in the 20–30 keV band. We note two striking features in the models, namely, the rapid onset of a high level of X-ray emission in both and the persistence of this emission for several hundred days in the case of UEC. These features are easily understood in terms of the extent of the radioactive source. Since the total optical depth corresponding to the entire diffusive path length of gamma rays which are to emerge as hard X-rays is ~ 5 (McCray *et al.* 1987), we can ask the question of where these gamma rays must be emitted within the ejecta to emerge a time t_d later, where t_d is the diffusion time. Calling this location ΔR from the instantaneous surface of the supernova, and estimating the electron density to be $n_e \approx 3MN_0/[4\pi(v_{\rm sc}\, t)^3]$, where N_0 is Avogadro's number, we obtain from the condition $\tau \approx 5 = n_e \sigma \Delta R$,

$$\frac{\Delta R}{R} \approx \frac{20\pi R^2}{3MN_0\sigma} \approx 4.4 \times 10^{-3}\left(\frac{M}{10M_\odot}\right)^{-1}\left(\frac{v_{\rm sc}}{3000\ {\rm km\ s^{-1}}}\right)^2\left(\frac{t}{50\ {\rm d}}\right)^2, \quad (5)$$

where here we have approximated $\sigma \approx \sigma_{\rm T}$. The corresponding diffusion time t_d is, approximately,

$$\frac{t_d}{t} \approx \frac{100\pi\beta R^2}{3MN_0\sigma} = 5\beta\,\Delta R/R \approx 2.2 \times 10^{-4}\left(\frac{\beta}{0.01}\right)\left(\frac{M}{10\ M_\odot}\right)^{-1}\left(\frac{v_{\rm sc}}{3000\ {\rm km\ s^{-1}}}\right)^2\left(\frac{t}{59\ {\rm d}}\right)^2, \quad (6)$$

where $\beta = v_{\rm sc}/c$. We note that both ΔR and t_d are remarkably small; even at $t = 350$ days, the $\tau = 5$ surface has only moved in to $x \approx 0.85$, and the corresponding diffusion time is ~ 2 days. Thus in model UEC, whose source is extended throughout, there is an early, rapid turn-on of X-rays at $t \approx 50$ days, at which time reprocessing of gamma-ray energies to X-rays is

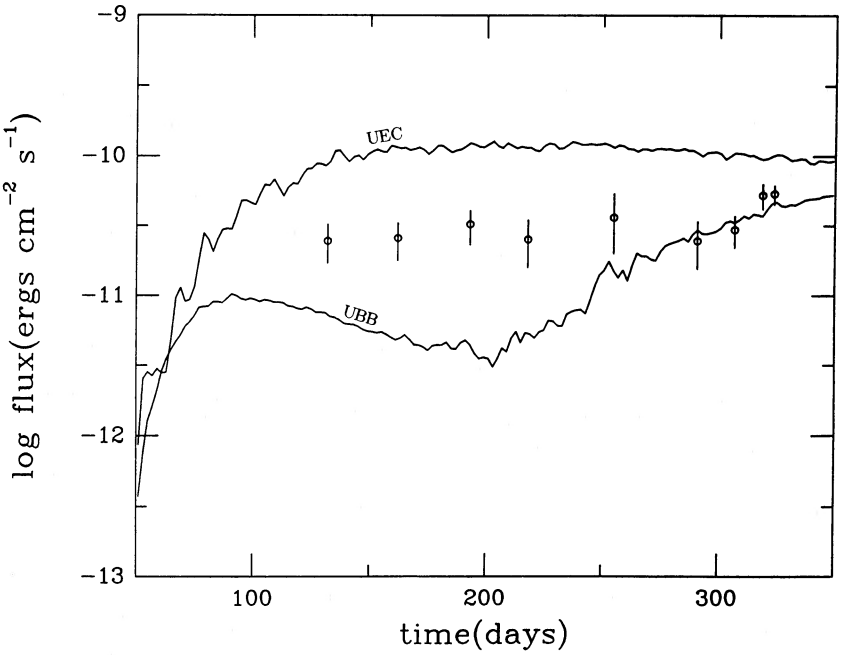

FIG. 3.—20–30 keV light curves for models UEC and UBB. Circles are the *Ginga* observations for the 16–28 keV flux, including estimated uncertainties. The large fluctuations when the flux level is low, due to statistical errors inherent in the Monte Carlo code, do not obstruct the overall shapes of the light curves.

nearly instantaneous. Subsequently, as the "clumps" are intercepted in sequence by the $\tau = 5$ surface, a lengthy persistence of this flux ensues.

Although the above analysis assumed that densities at the propagating diffusion front did not change appreciably during the diffusion, this is consistent with the result that t_d/t is small until late times—for homologous expansion, we have $\Delta n/n = -3\Delta t/t = -3t_d/t$. This stands in contrast to the analysis of McCray *et al.* (1987), who, by assuming a single physical depth to characterize X-ray emergence (i.e., a centrally condensed source), and a high velocity of $\sim 10{,}000$ km s^{-1}, estimated that X-ray emergence from the inner portion of the nebula should occur ~ 6 months after the explosion.

The *Ginga* observations for the integrated flux from 16 to 28 keV are also shown in Figure 3. As for the gamma-ray light curves, Figure 3 suggests that the distribution of radioactive mass lies somewhere in between the two extreme cases shown. The fact that the first detection occurs at 132 days may suggest that no significant amount of Co rises near the surface before this time (see, however, next paragraph). Indeed, the short X-ray diffusion times at this epoch invite some easy speculation about the characteristics of the hypothesized clumps. In general, it is difficult to obtain an analytic estimate of the X-ray flux since we must evaluate the "comoving" optical depth of photons diffusing in the expanding medium from source to surface. Here, however, $t_d/t \ll 1$; hence, that source which lies at $\tau \approx 5$ at a given time t produces X-rays at roughly the same epoch. Thus assuming that the fraction $1 - \exp(-\tau_\gamma)$ (where $\tau_\gamma \approx 0.3\tau_T$), which does not escape as prompt gamma rays, is downscattered to the X-ray regime, we have for the number luminosity of hard X-rays,

$$L_x \approx 4.5 \times 10^{47} \text{ s}^{-1} (M_{\rm Ni}/0.075\ M_\odot) \times \exp(-t/t_{\rm Co})[1 - \exp(-\tau_\gamma)] , \quad (7)$$

where $\tau_T \approx 5$ and $\tau_\gamma \approx 1.5$. At day 132 the 16–28 keV flux was $24.7(\pm 7.7) \times 10^{-12}$ ergs cm^{-2} s^{-1}, giving a number flux of $\sim 7.7 \times 10^{-4}$ cm^{-2} s^{-1}, with $\langle \epsilon \rangle = 20$ keV. Note that for $N \approx \tau_T^2 = 25$, emerging photons will have scattered $\sim 25 \pm N^{1/2} \approx 20$–$30$ times, giving emergent energies of ~ 17–25 keV, so that L_X as defined above can be directly compared to the *Ginga* flux. Assuming a distance of 55 kpc to the LMC, we obtain from equation (7), $M_{\rm Ni} \approx 1.9 \times 10^{-4}\ M_\odot$, $\sim 0.25\%$ of the total radioactive source, as that Co mass which gives rise to X-rays at 132 days. This much Co contributes an 847 keV flux of $F_\gamma \approx 7.4 \times 10^{-5}$ cm^{-2} s^{-1} (from the often stated analytic expression for the prompt gamma-ray line flux), which would be barely detectable by *SMM*, providing a possible explanation for the lack of a significant gamma-ray detection at the same time.

The persistence of this X-ray flux up to day 160, at which time the gamma rays were first detected, would also imply the persistent revelation (in X-rays, that is) of clumps of at least this size lying at progressively larger $\Delta R/R$. Since an 847 keV flux of $\sim 1.0 \times 10^{-3}$ cm^{-2} s^{-1} is equivalent to $\sim 0.97\%$ of the $0.075\ M_\odot$ source, at least roughly four to five clumps must pass through the $\tau = 5$ surface during this time to produce the required gamma-ray flux at 160 days; i.e., this much accumulated mass at zero optical depth at day 160 can produce the required level of flux. Because some nonzero depth probably characterizes this high-lying mass even at day 160, more material would probably be revealed at $\tau = 5$, either during the 28 day interval before day 160, or *before* day 132. (This last point may be important, since the detection at 132 days was the first *attempted* observation in a fairly contiguous series of attempts, and therefore may not signify the initial release of X-rays from the supernova.) In our calculations, we have replaced individual clumps by grouping of clumps within thin spherical shells of $\sim 1.5 \times 10^{-3}\ M_\odot$ of Co each, distributed uniformly throughout the nebula. (This larger mass per shell explains why the flux maximum of model UEC lies substantially above that detected by *Ginga*.) In a slightly more realistic representation, a given spherical shell of stellar material of thickness δr would contain an amount $\delta M_{\rm Ni}$ of radioactive mass and would be characterized by a filling factor f such that

$$4\pi r^2\, \delta r f \rho_{\rm cl} = \delta M_{\rm Ni} ,$$

where $\rho_{\rm cl}$ is the density of a clump within this volume. Here f is the product of a volume filling factor for the clumps times the mass fraction of Co within the clump; hence, $f\rho_{\rm cl}$ is the effective density of radioactive material in the ambient medium. We can take $\rho_{\rm cl} \leq \rho^*$, where $\rho^* = 3M/(4\pi R^3)$ is the ambient density, just the condition for the blob to have risen to a height r, $\delta M_{\rm Ni} \approx 1.9 \times 10^{-4}\ M_\odot$, $r \approx R$, and $\delta r/R \approx 0.2 \times 10^{-2}$, which is consistent with the idea that the $\tau \approx 5$ surface must move through $\Delta R/R \approx 1 \times 10^{-2}$ from the time of x to gamma-ray emergence in order to uncover enough (roughly four to five) clumps of Co as explained above. We thus obtain

$$f \approx \delta M_{\rm Ni}/(3M)(\delta r/R)^{-1} = 2.8 \times 10^{-3} ,$$

for $M = 11.15\ M_\odot$. Such a distribution could exist over a substantial region of the outer envelope, since if we defined $r_{\rm Ni}$ such that

$$4\pi/3 f \rho_{\rm cl}\, r_{\rm Ni}^3 = M_{\rm Ni} ,$$

we would find that

$$r_{\rm Ni}/R = [M_{\rm Ni}/(fM)]^{1/3} = 1.34$$

for $M_{\rm Ni} = 0.075\ M_\odot$. Therefore, some central condensation of radioactive material would exist, as one might expect, at the times over which the X-ray flux remains approximately steady, and indeed the X-ray "flare" observed by *Ginga* on day 319 (Makino 1987*a*, *b*, *c*) might be due to the coincidence of the $\tau \approx 5$ surface (a few days earlier) with a rise in effective radioactive mass density (see Fig. 3).

We tentatively conclude, if the mass and velocity chosen from the aggregate of theoretical and observational constraints discussed above are in the correct range, that *a $0.075\ M_\odot$ radioactive source condensed within the helium core could not have produced the X-rays detected by Ginga thus far*. This argument is independent of the actual amount of radioactive mass which gave rise to the flux, since the optical depth alone determines at which energies the photons emerge. (For instance, even though model UBB has $7.5 \times 10^{-4}\ M_\odot$ of Co in an extended shell, Figure 3 shows that its extreme proximity to the surface makes it incapable of ever achieving a level of hard X-ray flux equal to that detected by *Ginga*.) The alternative assumption of an extended source, however, combined with the fact that diffusion times for X-ray emergence from such a source are short throughout the first year of evolution, means that we can, as we have done, estimate the mass of clumped Co which generates the X-ray luminosity from the detected level of flux.

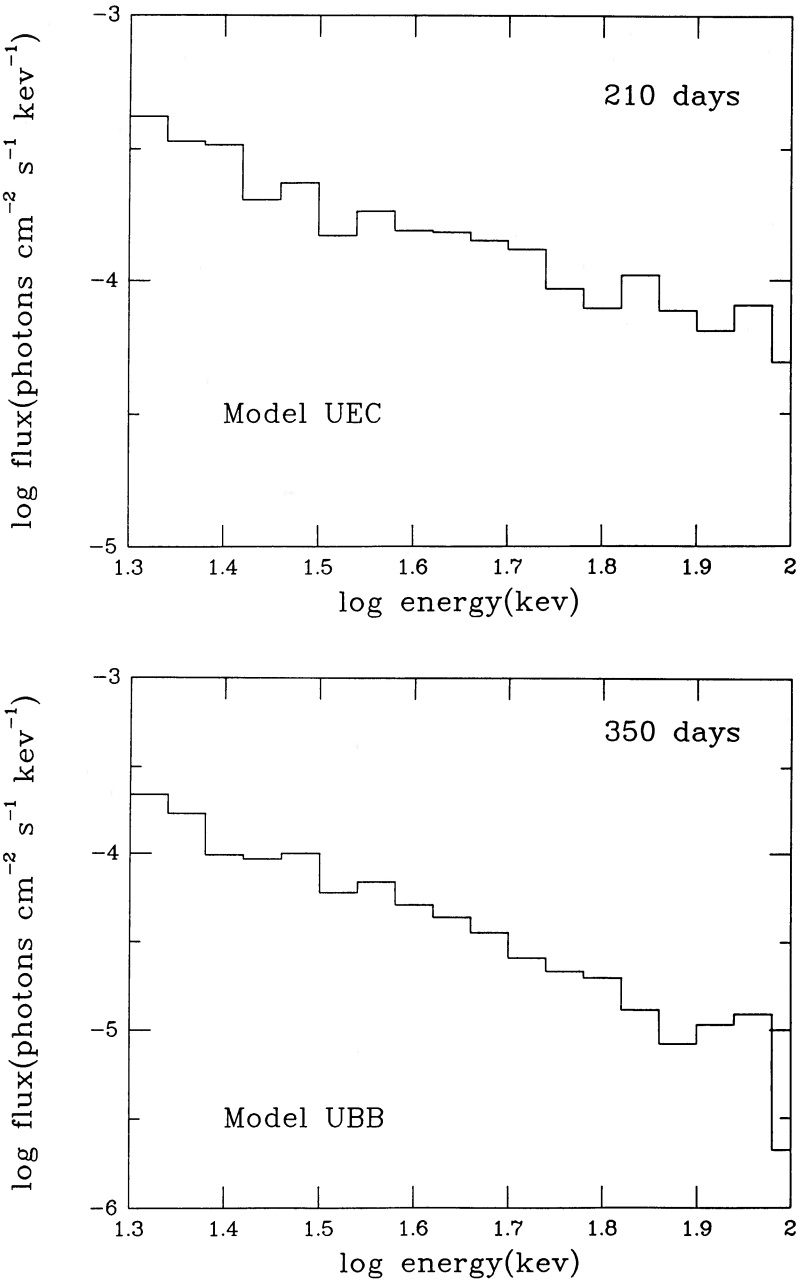

FIG. 4.—Comptonized gamma-ray continuum spectra in the range 20–100 keV for models (*a*) UEC and (*b*) UBB at the approximate times of their respective maxima in 20–30 keV X-rays. Bin size is $\Delta E/E = 0.096$, large enough to partially compensate for statistical errors due to the small photon samples used, yet small enough to obtain reasonable least-squares fits to the continuum slope.

c) X-Ray Spectra

Figures 4*a* and 4*b* show Comptonized gamma-ray spectra from 20 to 100 keV for models UEC and UBB, respectively, at the approximate times of maximum hard X-ray luminosity for the two models. Although the continua were rough because of the small number of photons emitted in the simulations, we have made least-squares fits to the spectra in order to determine the evolution of the spectral slope, and these have yielded reasonable and interesting results. Previous models with a centrally condensed source have naturally produced a steady hardening of the continuum with time. In Figure 5*a*, model UEC also displays a secular hardening of the spectrum over the period 150–350 days, even though, as shown in Figure 3, the X-ray luminosity remains steady during this time. As the $\tau = 5$ surface (the X-ray "transparency wave") moves in, more and more material which must scatter less and emit at shorter wavelengths is left in its wake. A residual hard component thus builds slowly in time, although this long-term hardening is slower than for a centrally condensed source due to the competing effect of softening of the spectrum by material emitting at optical depths close to ~ 5. Contrary to this secular trend is an episode of spectral softening in UEC from 210 to 310 days. Although this might be due to statistical errors inherent in our Monte Carlo calculation, it is more likely a systematic effect

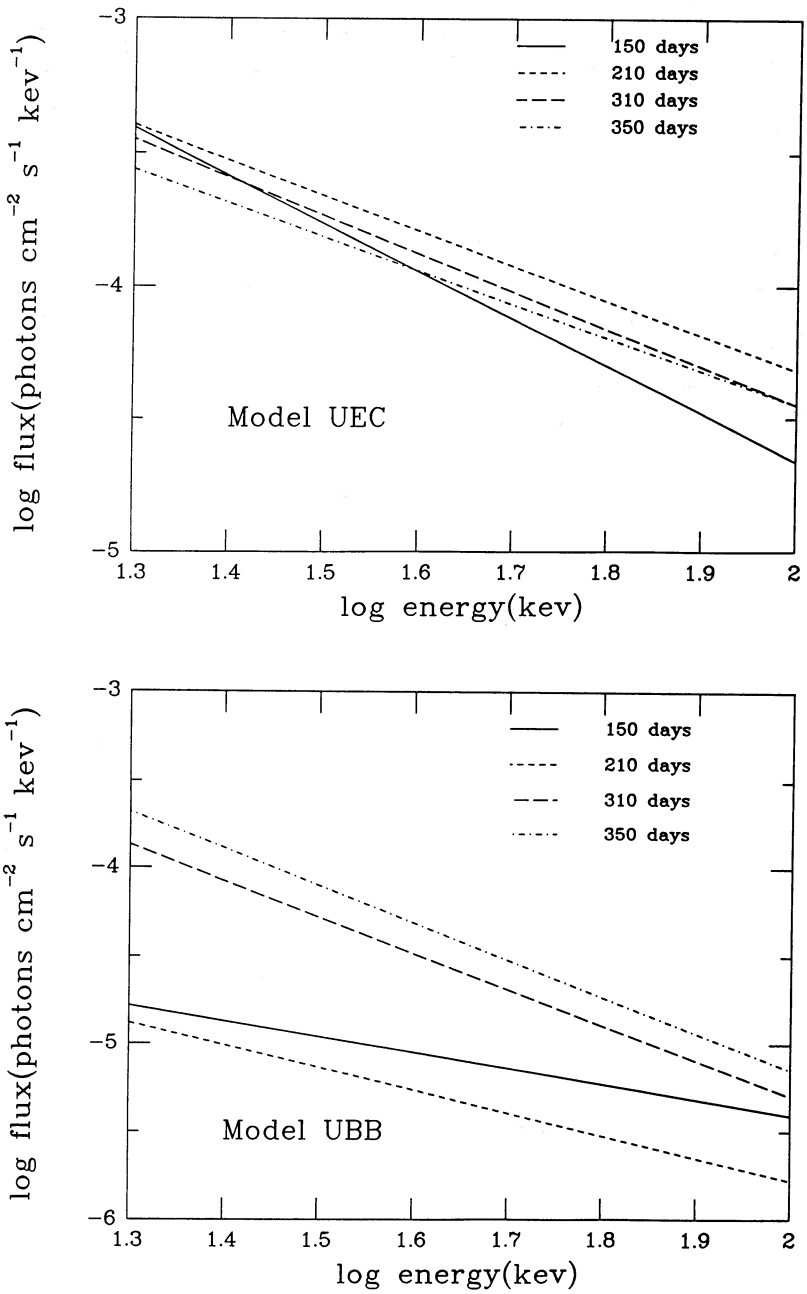

FIG. 5.—Evolution of least-squares fits to the spectra (as in Fig. 4) for models (*a*) UEC and (*b*) UBB, respectively. The spectra at 150, 210, 310, and 350 days are shown. For UEC, the slopes are, approximately, −1.79(150 days), −1.32(210 days), −1.43(310 days), and −1.27(350 days); for UBB, they are −0.90(150 days), −1.28(210 days), −2.04(310 days), −2.10(350 days).

built into our representation of the extended source—since the source is distributed in discrete shells, the spectrum may harden when the X-ray transparency wave passes between shells only to soften again as it suddenly coincides with the next shell. Such episodic behavior of the continuum may not be unreasonable to expect from the supernova, depending on how the radioactive bubbles develop in time.

Figure 5*b* shows how the bulk source in model UBB progressively dominates the continuum, beginning at ~210 days. The hard spectrum at 150 days displays the waning of the small clumped source, whose X-ray peak occurred ~50 days earlier. As seen in Figure 3, the much more massive bulk source begins to swamp the shell source after ~200 days, and consistently begins to soften the spectrum at day 210. Both the X-ray luminosity and spectral softness then steadily rise, as the X-ray transparency wave moves in toward the edge of the helium core at $x = 2100/2580 = 0.813$, reaching it and a peak luminosity at ~350 days, which is consistent with equation (5).

d) Optical Fit

In Figure 6, we show the optical light curve for $M = 11.15\ M_\odot$ and $v_{sc} = 2580$ km s^{-1}, using the methods of Paper II.

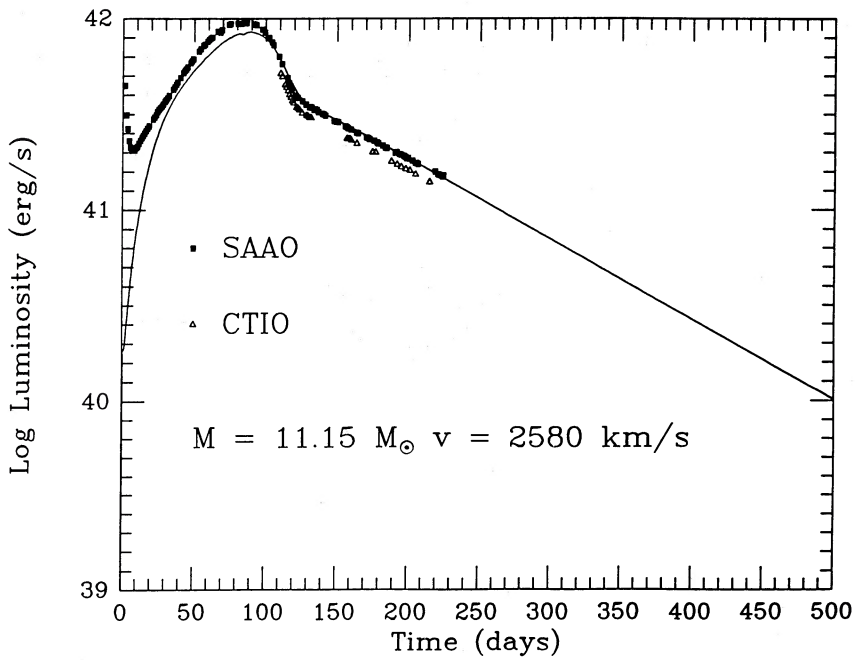

FIG. 6.—Optical fit for $M = 11.15\ M_\odot$, and $v_\kappa = 2580$ km s^{-1}, the values used in models UEC and UBB. Observed points from the CTIO and SAAO data sets are also shown.

Also plotted are the observational data from the SAAO group (Menzies *et al.* 1987, 1988). The fit is good and is similar to those models investigated in Paper II, which have slightly different values for M and v_{sc}. The extent of the radioactive source has no effect on the optical light curve until ~ 1 yr after the explosion. The reported sag in the optical light curve, reaching $\sim 7\%$ on day 340 (Catchpole and Whitelock 1988) seems to support the idea of an extended source. This issue has been addressed in Paper II. Hence, beginning at the present time, further model development aimed toward understanding the high-energy behavior of the event must also address the optical behavior in more detail.

e) Geometric Effects of the Extended Source

The radiative transfer calculations with uniform density are particularly useful in quantifying the geometric effects of an extended radioactive source. Figure 7 shows analytic 847 keV light curves for with bulk sources for $x_{Ni} = 1.0, 0.8, 0.6, 0.4, 0.2$, and 0.001, in this case with $M = 15.6\ M_\odot$ and $v_{sc} = 2887$ km s^{-1}, values also consistent with the velocity at the edge of the 6 $M_\odot$ helium core. The parameterization in x_{Ni} cuts off at $x_{Ni} = 0.1$, as expected from the $1 - x_{Ni}$ dependence of the optical depth. Monotonically decreasing density profiles yield smaller cutoff values of x_{Ni}. Figure 7 also shows how the time and level of maximum flux depend on the factor $1 - x_{Ni}$. As has been amply stated in other works, the gamma-ray luminosity roughly depends on $\tau_R(t)$ as $\exp[-\tau_R(t)]$; hence, the maximum luminosity has the dependence $\exp[-b(1 - x_{Ni})^{1/3}]$, where the constant b depends on mass, velocity, and composition. The time of maximum then can be easily shown to have the dependence $(1 - x_{Ni})^{1/3}$. In Figure 7, these dependences hold for small x_{Ni}, but for $x_{Ni} \gtrsim 0.4$, significant deviations from these simplified formulae can be seen, the maxima occurring later and at a lower level than predicted. These trends are obvious consequences of obtaining a broader range of radial depths which characterize the gamma-ray escape as the extent of the source increases.

Another significant effect of the extended source is that it produces a range of optical depths in angle at each radius. Figure 8 shows a comparison of analytic and numerical light curves for $x_{Ni} = 0.6, 0.3, 0.1$, and 0.001, and the same mass and velocity as in Figure 7. The analytic models begin to differ significantly from the simulations for $x_{Ni} \gtrsim 0.1$, yielding enhanced transparency at earlier times and higher maxima. As explained in Paper II, the outward and inward radial optical depths for material located at x are $\tau_+ = \tau_c(1 - x)$ and $\tau_- = \tau_c(1 + x)$, respectively, where τ_c is the optical depth to the center. Therefore, when we ignore the obliquity of rays in the analytic model, we underestimate the mean outwardly directed optical depth and overestimate the mean inwardly directed optical depth. Figure 8 merely shows that for a sufficiently extended source, $x_{Ni} \geq 0.1$, this former error is more serious than the latter, whereas for $x_{Ni} \leq 0.1$, both errors are insignifi-

V. CONCLUSIONS

We have constructed models for the gamma-ray radiative transfer which are consistent with important constraints on the specific explosion energy, and the mass and velocity of the helium core, and which employ all the significant physical elements of the successful optical model for the light curve of SN 1987A. Within the context of our models, it is likely that the current gamma-ray observations can be explained by the "effervescence" of radioactive bubbles in the upper layers of the ejecta. The progressive transparency of these bubbles, both by their buoyancy and thinning of the surrounding medium, also provides a natural explanation for the early detection and persistent level of hard X-ray flux as observed by *Ginga*. We eagerly await future high-energy observations in order to confirm or deny this scenario.

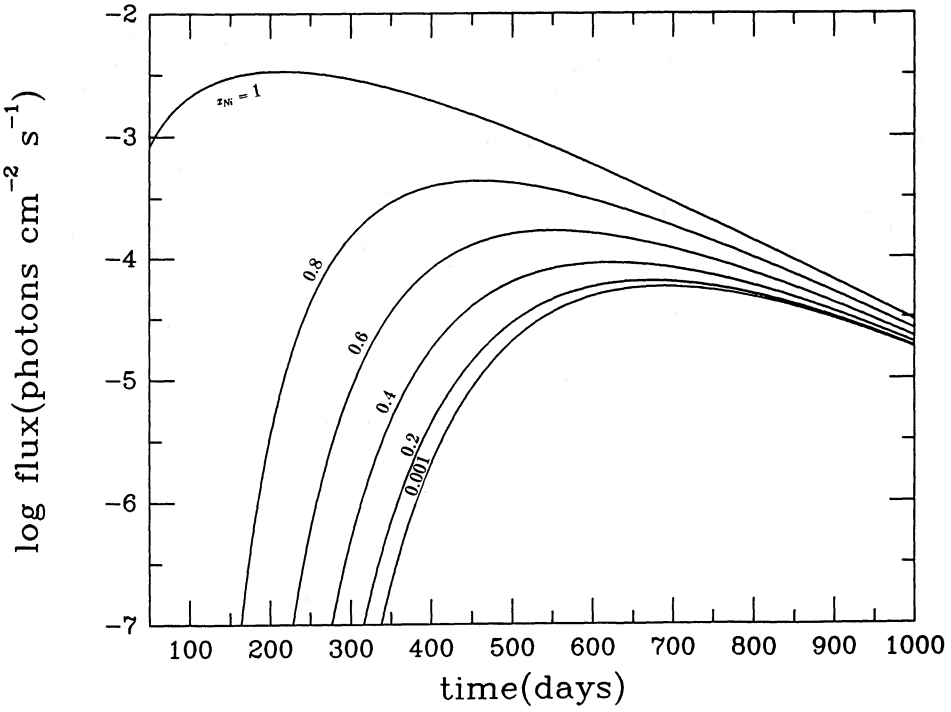

FIG. 7.—Analytic light curves for the 847 keV line for $M = 15.6\,M_{\odot}$, and $v_{sc} = 2887$ km s^{-1}, and for $x_{Ni} = 1$, 0.8, 0.6, 0.4, 0.2, and 0.001

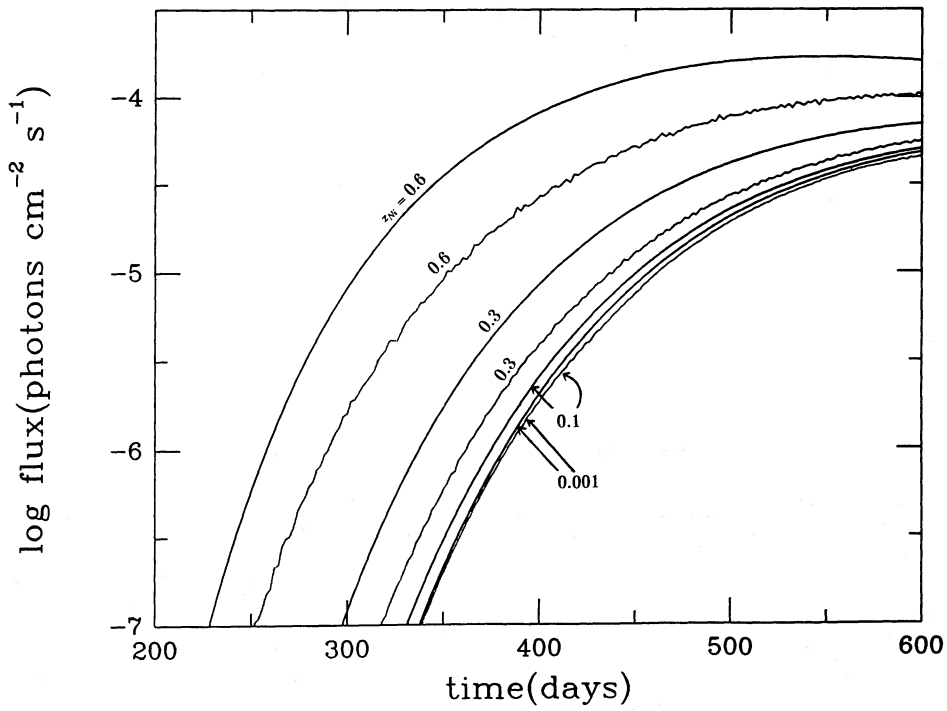

FIG. 8.—Comparison of analytic (*solid*) and numerical (*dotted*) 847 keV light curves for the same mass and velocity as in Fig. 7 for $x_{Ni} = 0.6$, 0.3, 0.1, and 0.001. The numerical curves for $x_{Ni} = 0.1$ and 0.001 are essentially identical.

We have arrived at conclusions similar to those of Paper II concerning the high-energy observations, although from a different point of view. There, we chose the parameters M and v_{sc} on the basis of the numerical results of Paper I. Here we used the observational and theoretical constraints on the edge of the helium core to find suitable values of M and v_{sc}. Hence, the former approach did not position the edge of the helium core consistently with a linear velocity space, although this constraint cannot be regarded as stringent, which underlies the deficiency in the latter approach as a means for choosing very specific values of these parameters despite the firmness of our knowledge concerning M_{He}, v_{He}, and E_{SN}/M. Nevertheless, both approaches result in the important conclusion that very extensive mixing of the NiCo in the ejecta is strongly suggested by the high-energy observations. Only very highly transparent ($M \lesssim 8\ M_\odot$, $v_{sc} \gtrsim 4800$ km s^{-1}) models can yield the early emergence of high-energy radiation as observed *without mixing beyond the edge of the helium core*, but these also yield levels of long-term X-ray and gamma-ray luminosity substantially higher than observed, and more importantly, produce a premature sag in the optical light curve which we know with considerably less uncertainty.

The very suggestion that the results point to an evolutionary development of blobs means that any one model is incapable of representing the real supernova, since it has a fixed NiCo distribution in velocity space. However, we have made clear the importance of the NiCo distribution, and have also emphasized the importance of the density profile, both of which, at the interesting times, are consequences of the development of the Rayleigh-Taylor instability as found in the earlier numerical experiments. A combination of complex kinematic effects and a complicated mass distribution, both of which are nonspherical in nature, are probably important. A clear picture of this development is vital for a complete understanding of the high-energy observations.

Hydrodynamic calculations in progress (Fryxell and Arnett 1988) should be the key step toward realizing this goal.

The authors wish to thank Professors Ronald E. Taam, Don Q. Lamb, Melville P. Ulmer, and Thomas Loredo and John Wang for extremely helpful discussions. This work was supported by NSF grants AST8608291 to Northwestern University, AST8519968 to the University of Chicago, and by NASA grant NAGW-768 to Northwestern University.

REFERENCES

Arnett, W. D. 1980, *Ap. J.*, **237**, 541.
———. 1982, *Ap. J.*, **253**, 785.
———. 1987, *Ap. J.*, **319**, 136 (Paper I).
———. 1989, in preparation.
Arnett, W. D., and Fu, A. 1989, *Ap. J.*, **340**, 396 (Paper II).
Catchpole, R. M., *et al.* 1988, *M.N.R.A.S.*, **229**, 15P.
Catchpole, R. M., and Whitelock, P. A. 1988, *IAU Circ.*, No. 4544.
Chan, K. W., and Lingenfelter, R. E. 1987, *Ap. J. (Letters)*, **318**, L51.
Cook, W. R., Palmer, D., Prince, T., Schindler, S., Starr, C., and Stone, F. 1988, *IAU Circ.*, No. 4527.
Dotani, T., *et al.* 1987, *Nature*, **330**, 230.
Ebisuzaki, T., and Shibazaki, N. 1988, *Ap. J. (Letters)*, **327**, L5.
Falk, S. W., and Arnett, W. D. 1973, *Ap. J. (Letters)*, **180**, L65.
Fransson, C., and Chevalier, R. A. 1987, *Ap. J. (Letters)*, **322**, L15.
Gehrels, N., MacCallum, C. J., and Leventhal, M. 1987, *Ap. J. (Letters)*, **320**, L19.
Itoh, M., Kumagai, S., Shigeyama, T., Nomoto, K., and Nishimura, J. 1987, *Nature*, **330**, 233.
Lucy, L. 1987, *Astr. Ap.*, **182**, L31.
Makino, F. 1987*a*, *IAU Circ.*, No. 4447.
———. 1987*b*, *IAU Circ.*, No. 4530.
———. 1987*c*, *IAU Circ.*, No. 4532.
Matz, S. M., Share, G. H., Leising, M. D., Chupp, E. L., Vestrand, W. T., Purcell, W. R., Strickman, M. S., and Reppin, C. 1988, *Nature*, **331**, 416.
McCray, R., Shull, J. M., and Sutherland, P. 1987, *Ap. J. (Letters)*, **317**, L69.
Phillips, M., *et al.* 1989, in preparation.
Pinto, P. A., and Woosley, S. E. 1988, *Ap. J.*, **329**, 820.
Rester, A. C., Eichhorn, G., and Coldwell, R. L. 1988, *IAU Circ.*, No. 4535.
Sandie, W., Nakano, G., and Chase, L. 1988, *IAU Circ.*, No. 4526.
Shigeyama, T., Nomoto, K., Hashimoto, M., and Sugimoto, D. 1987, *Nature*, **328**, 320.
Shull, J. M., and Xu, Y. 1988, in *Supernova 1987A in the Large Magellanic Cloud: Proc. of the Fourth George Mason Astrophysics Workshop*, ed. M. Kafatos and A. G. Michalitsianos (Cambridge: Cambridge University Press), p. 371.
Sonneborn, G., and Kirshner, R. 1987, preprint.
Woosley, S. E., Pinto, P. A., and Ensman, L. 1988, *Ap. J.*, **324**, 466.
Woosley, S. E. 1987, preprint.

W. David Arnett: Enrico Fermi Institute, the University of Chicago, Chicago, IL 60637

Albert Fu: Dearborn Observatory, Department of Physics and Astronomy, Northwestern University, Evanston, IL 60202